EINDHOVEN
UNIVERSITY OF
TECHNOLOGY

Eindhoven University of Technology

MASTER

Atomic layer deposition of ZnO and Al-doped ZnO

Hermkens, P.M.

Award date:
2012

Link to publication

Disclaimer
This document contains a student thesis (bachelor's or master's), as authored by a student at Eindhoven University of Technology. Student theses are made available in the TU/e repository upon obtaining the required degree. The grade received is not published on the document as presented in the repository. The required complexity or quality of research of student theses may vary by program, and the required minimum study period may vary in duration.

General rights
Copyright and moral rights for the publications made accessible in the public portal are retained by the authors and/or other copyright owners and it is a condition of accessing publications that users recognise and abide by the legal requirements associated with these rights.

- Users may download and print one copy of any publication from the public portal for the purpose of private study or research.
- You may not further distribute the material or use it for any profit-making activity or commercial gain

Technische Universiteit
Eindhoven
University of Technology

Department of Applied Physics
Plasma & Materials Processing group (PMP)

Atomic layer deposition of ZnO and Al-doped ZnO

P.M. Hermkens B.Sc.

July 2012
PMP …

Supervisors:
dr. S.E. Potts
Prof.dr.ir. W.M.M Kessels

Abstract

As a *transparent conducting oxide* (TCO) or a transparent semiconductor, *Zinc oxide* (ZnO) is a promising candidate for many existing and novel thin film applications. *Atomic layer deposition* (ALD) exhibits excellent uniformity, conformality and thickness control and is therefore a suitable method for producing such ZnO thin layers. The first part of this thesis concerned the ALD process development and characterization of ZnO. The thermal process showed a good *growth per cycle* (GPC) of 0.21 nm/cycle, non-uniformity of 3.3 % and minimum resistivity in the order of 10^{-2} Ωcm for 40 nm thick films. The plasma-assisted process gave a GPC of 0.09 nm/cycle, non-uniformity of 22.3 %, a minimum resistivity in the order of 10^{1} Ωcm for 40 nm thick films and required a long plasma dose of 16 s before saturation was reached. These latter results were not optimal for most applications and therefore this process needs to be further optimized before the full potential of the plasma-assisted ALD process can be utilized.

The second part of this thesis concerned the doping of ZnO with aluminium. Thermal ALD processes were developed using both *trimethyl-aluminium* (TMA) and *dimethyl-aluminium isopropoxide* (DMAI) as Al precursors. Minimum resistivities in the order of 10^{-3} Ωcm were achieved for films of 40 nm thickness at an Al fraction of approximately 3 %, even without optimizing the deposition temperature. The use of TMA and DMAI showed growth inhibition of subsequent ZnO cycles in both cases. This effect however, was more pronounced for DMAI. The reason was hypothesized to be the passivation of surface OH groups and shielding of adjacent OH groups (steric hindrance) by remaining isopropoxide ligands. DMAI showed higher doping efficiency and lower resistivity than TMA at equal Al fractions. This was ascribed to the large DMAI ligands, which by steric hindrance, cause the Al atoms to be more sparsely located throughout the material. Therefore the coulomb repulsion between donated electrons, which suppresses further electron donation, was less attenuated.

Contents

CHAPTER 1: INTRODUCTION 7

1.1 TRANSPARENT CONDUCTING OXIDES 8
1.2 ZINC OXIDE 10
1.3 ATOMIC LAYER DEPOSITION 11
1.4 PROJECT GOALS 13
1.5 THESIS OUTLINE 14

CHAPTER 2: DEPOSITION & DIAGNOSTIC TECHNIQUES 15

2.1 ALD REACTOR 15
2.2 PRECURSORS 16
2.3 SPECTROSCOPIC ELLIPSOMETRY 17
2.4 FOUR-POINT PROBE 18
2.5 HALL SYSTEM MEASUREMENTS 19
2.6 RUTHERFORD BACKSCATTERING SPECTROSCOPY/ELASTIC RECOIL DETECTION 20
2.7 X-RAY PHOTOELECTRON SPECTROSCOPY STUDY 21
2.8 X-RAY DIFFRACTION 21

CHAPTER 3: PROCESS DEVELOPMENT & CHARACTERIZATION OF INTRINSIC ZINC OXIDE 23

3.1 PROCESS DEVELOPMENT 23
3.1.1 EXPERIMENTAL DETAILS OF PROCESS DEVELOPMENT 23
3.1.2 RESULTS AND DISCUSSION OF PROCESS DEVELOPMENT 25
3.2 INTRINSIC ZINC OXIDE MATERIAL CHARACTERIZATION 32
3.2.1 EXPERIMENTAL DETAILS OF INTRINSIC ZINC OXIDE CHARACTERIZATION 32
3.2.2 GROWTH PER CYCLE AS A FUNCTION OF DEPOSITION TEMPERATURE 33
3.2.3 MATERIAL PROPERTIES MEASURED BY RBD/ERD 35
3.2.4 NON-UNIFORMITY 37
3.2.5 ELECTRICAL RESISTIVITY 38
3.2.6 TRANSMITTANCE 41
3.2.7 OPTICAL BAND GAP 42
3.2.8 CRYSTALINITY 44
3.3 CONCLUSIONS AND OUTLOOK 45

CHAPTER 4: ALUMINIUM DOPING OF ZINC OXIDE 46

4.1 INTRODUCTION 46
4.1.1 LITERATURE OVERVIEW OF ALUMINIUM DOPED ZNO BY ALD 46
4.1.2 ALUMINIUM PRECURSORS 49
4.1.3 MEASURING AL FRACTION WITH SPECTROSCOPIC ELLIPSOMETRY 50
4.1.4 GOALS 51
4.2 EXPERIMENTAL 52
4.3 ZNO GROWTH DELAY AFTER AL_2O_3 CYCLE 53

4.4 ALUMINIUM FRACTION 59
4.5 ELECTRICAL PROPERTIES 61
4.5.1 MEASUREMENT RESULTS 61
4.5.2 FIELD EFFECT MODEL 63
4.5.3 DOPING EFFICIENCY 65
4.6 OPTICAL PROPERTIES 69
4.6.1 TRANSMITTANCE 69
4.6.2 OPTICAL BAND GAP 69
4.6.3 SPECTROSCOPIC ELLIPSOMETRY MATERIAL LIBRARY 72
4.7 CONCLUSIONS AND OUTLOOK 73

CHAPTER 5: CONCLUSIONS AND OUTLOOK 75

ACKNOWLEDGEMENTS 77

APPENDIX A: PRECURSOR PROPERTIES 79

APPENDIX B: RECIPES OF ZNO & AL_2O_3 PROCESSES 81

BIBLIOGRAPHY 85

Chapter 1

Introduction

Zinc oxide (ZnO) is a versatile material. It was already produced in the Bronze age when it was used for the healing of wounds [1]. Modern day industrial applications comprise chemicals, white paints, ceramics, cosmetics and rubber [1].

The research on ZnO as a semiconductor material started in the middle of the 20th century and was relatively intensive in the 1950s and 1970s [1]. However, a significant increase in the number of publications on ZnO started around 1990. This is shown by Figure 1.1 [1,2]. An important factor that triggered this renewed interest in ZnO, was the progress in nanostructure fabrication techniques [1,2]. New methods were developed that could be used to produce structures on the nm scale. ZnO, as a semiconductor, has many (potential) applications in nanostructures. General examples are ZnO as [1-6]:

- *Transparent conducting oxide* (TCO). TCOs are applied as transparent electronic contacts in solar cells, flat panel displays and touch panels. Another emerging application is ZnO as a channel layer in *transparent thin film transistors* (TTFTs). Electrical conductivity and transparency for visible light are important TCO properties;
- Junction material or as junction material compound in heterojunction *light emitting diodes* (LEDs). ZnO is suitable for this application because it exhibits n-type conductivity. ZnO in heterojunction LEDs is currently an emerging application. In the future ZnO can possibly be used in homojunction LEDs as well. For this to be possible however, p-type conductivity will be necessary;
- Active material in chemical and gas sensors. The surface resistivity of ZnO depends strongly on adsorbed species. This can be used in sensing devices. The sensitivity of such devices improves with increasing surface to volume ratio. The ZnO layers in these devices are therefore required to be as thin as possible;
- Piezoelectric devices such as mechanical sensors and *micromechanical systems* (SEMS), since ZnO is a piezoelectric material;
- Ferromagnetic material in spintronics since ZnO can act as a ferromagnetic material when doped with magnetic ions;

TCO production is currently the largest application of thin film ZnO. The focus of this thesis will therefore be on the electrical and optical properties of ZnO.

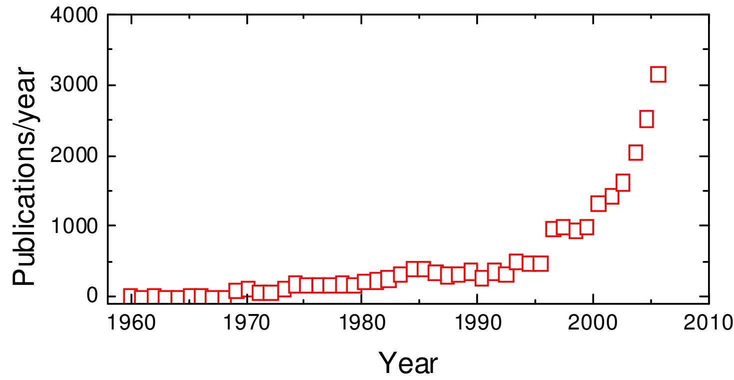

Figure 1.1 *Increase of the number of publications about zinc oxide (ZnO) over the last decades* [1]

1.1 Transparent Conducting Oxides

TCOs are metal oxides that are used in optoelectronic devices. A TCO combines the property of conductivity with transparency in a specific wavelength region. The transparent wavelength region is determined by the material bandgap. Figure 1.2 shows an example of a TCO in a *heterojunction with intrinsic thin layer* (HIT) solar cell, where it acts as transparent contact that transports charge carriers to the metal contacts.

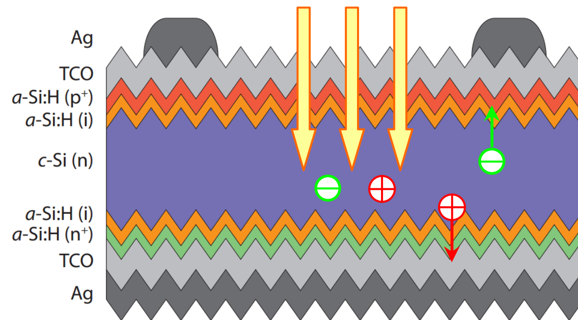

Figure 1.2 *Schematic representation of a HIT solar cell. Sunlight enters the device by passing through the TCO. The sunlight then creates free charges in the c-Si (n) layer. The free charges are transported through the TCO to the metal contacts. Picture used from de Wolf et al. [7].*

Important TCO requirements are [1,8]:

- High transparency (> 80%) in the spectral region of interest. Typically in the visible and near infrared region;
- Low resistivity (< 10^{-3} Ω cm). The resistivity for a n-type material is determined by both the free electron density and the electron mobility [9]:

$$\rho = \frac{1}{q \cdot n \cdot \mu_n} \quad (1.1)$$

Where ρ is the resistivity, q the elementary charge, n the free electron density and μ_n the electron mobility. A high free electron density causes the material to be less transparent, mainly in the infrared region. Therefore, low resistivity values are mainly required to be caused by high mobility values instead of high electron density.

- The possibility to be deposited at low substrate temperature (< 200 °C for HIT solar cells);
- (Tunable) roughness, which can be required in solar cells for light trapping;
- High abundance of composing materials and low material costs.

The most widely applied TCO is *Indium tin oxide* (ITO), $In_2O_3{:}Sn$ [1,8,10,11]. ITO can be deposited with resistivity values in the order of 10^{-4} Ωcm while exhibiting a transmittance above 80 % in the spectral range between 400 and 2000 nm. Indium however, is a scarce material that causes the material to be expensive [1]. For this reason other materials are being searched that can be used as TCO.

ZnO is a promising candidate for many existing and novel TCO applications. It has a high direct bandgap of approximately 3.2 eV, which makes it transparent for wavelengths above approximately 387 nm. Excellent resistivities down to 10^{-4} Ω cm have been reported for doped ZnO, while keeping the transmittance above 80 % in the visible wavelength region [12,13]. Doping however, is required to reach these low resistivities, as will be described later. Reported dopants are Al, Ga, In, B and F [4-6,8]. ZnO can be etched to tune the roughness after deposition [1]. The material is abundant and thus relatively cheap compared to indium.

1.2 Zinc Oxide Material Properties

ZnO crystallizes in two main forms, hexagonal wurtzite as shown in Figure 1.3 and cubic zincblende. The wurtzite structure is most stable under ambient conditions like room temperature and atmospheric pressure [1,3,6].

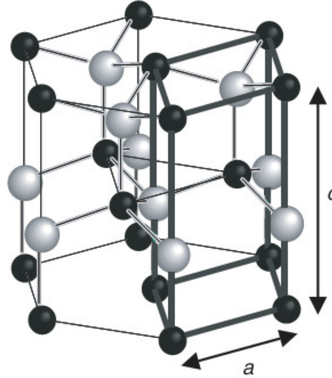

Figure 1.3 *Schematic representation of the wurtzite structure lattice placed within a hexagonal prism. The black atoms are Zn and the grey atoms are O. The lattice constants are a= 0.325 nm, c=0.52066 nm* [1].

ZnO exhibits an n-type character caused by intrinsic point defects [1]. Intrinsic point defects are deviations from the ideal crystal structure that are caused by displacement or removal of lattice atoms. Possible intrinsic defects are vacancies and interstitials. Historically, it was believed that *zinc interstitials* (Zn_i) and *oxygen vacancies* (V_O), shown in Figure 1.4, were the main cause of the n-type conductivity [5,14]. In this assumption the oxygen vacancies act as shallow acceptors and play the most dominant role in n-type conductivity [5,14]. The assumption was based on the existing relationship between resistivity and the partial O pressure during deposition or annealing, which was observed in many studies. Modern day theoretical calculations show however, that V_O only acts as deep donor. V_O can therefore not be the dominant contribution to the n-type conductivity. Other defects are likely to be more important. The debate on this topic is still going on but there seems to be some evidence that interstitial or substitutional hydrogen acts as dominant shallow donor [3,5,14]. This is also shown in Figure 1.4.

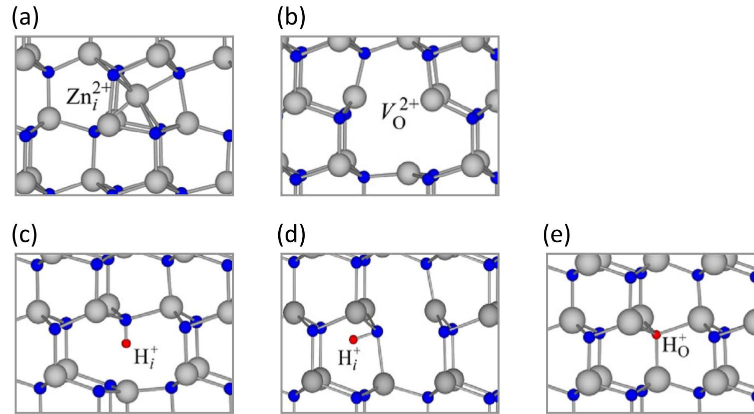

Figure 1.4 *Schematic representation of defects in the ZnO crystal: (a) Zinc interstitial (b) Oxygen vacancy. (c) Hydrogen interstitial at the bond- center site parallel to the c-axis. (d) Hydrogen interstitial at the anti-bonding site perpendicular to the c-axis. (e) Hydrogen at the substitutional oxygen site [5].*

For ZnO, doping is required to achieve sufficiently low resistivities for use in opto-electronic devices. Doping is the substitution of Zn atoms by group-III elements such as Al, B, Ga or In. These elements act as shallow donor and donate an electron into the conduction band.

There are several successful deposition techniques for thin layer ZnO. Examples are magnetron sputtering, *chemical vapour deposition* (CVD), *pulsed laser deposition* (PLD), atomic layer deposition, molecular beam epitaxy, spray pyrolysis and electro chemical deposition [1]. This thesis focuses on atomic layer deposition.

1.3 Atomic Layer Deposition

Atomic layer deposition (ALD) [15-19] is a thin film deposition technique that exhibits excellent uniformity, high conformality on high aspect ratio structures and precise thickness control. This is depicted in Figure 1.5. To understand the origin of this nature it is illustrative to explain the ALD process with Figure 1.6.

ALD typically consists of two self limiting half-cycles. In the first half-cycle a vapour of metal-organic or metal-halide precursor is dosed and adsorption of precursor molecules on available surface sites takes place. This exposure step is followed by a purge step to remove the volatile reaction products and the excess of unreacted precursor molecules. The second half cycle is an exposure to an oxidizing or reducing reactant to remove the

ligands from the metallic centre and obtain the desired material. This exposure is again followed by a purge step to remove reaction products. The two half-cycles make up the ALD cycle and the ALD cycles are repeated until the targeted thickness is reached. Doped materials can be deposited by alternating between ALD cycles of different materials.

Films that are grown by ALD are highly uniform and yield excellent conformality because one precursor/oxidizing molecule can adsorb at every available surface site regardless of the incoming particle flux. This insensitivity to the particle flux is only achieved when all available surface sites have reacted by receiving at least a certain number of particles. That is, the surface reactions should have reached saturation. In practice this means that the precursor dosing times must be long enough. Besides this the purge times must be long enough as well since CVD-like reactions can take place when precursor and oxidizing molecules are present in the reactor at the same time. Optimizing an ALD process comprises the determination of the minimum values of precursor dosing times and purge time steps.

ALD processes can be categorized in thermal ALD and energy-enhanced ALD. With thermal ALD the reactant is a gas or vapour such as O_2 or H_2O and the chemical reactions are driven by thermal energy. ALD processes in which the reactivity of the precursors is enhanced by adding other forms of energy are called energy-enhanced ALD processes. Examples of energy-enhanced reactants are ozone or plasma (plasma-assisted ALD). The radicals or other energetic species in energy-enhanced ALD help to induce reactions that are not possible with just thermal energy. The potential merits which of energy-enhanced ALD are improved material properties, deposition at reduced substrate temperatures, increased choice or precursors and materials, good control of stochiometry and film composition, increased growth rate, more processing versatility in general [16].

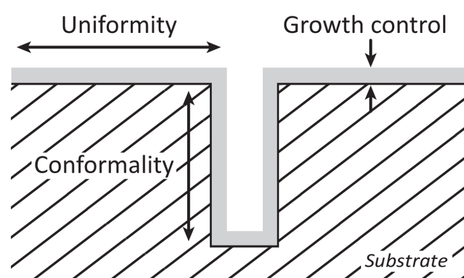

Figure 1.5 *Schematic visualization of the key advantages of ALD over other deposition techniques. ALD is a layer-by-layer deposition method that enables precise growth control. Due to the self limiting nature of the surface reactions the method produces highly uniform layers. This uniformity can even be maintained in high aspect ratio structures.*

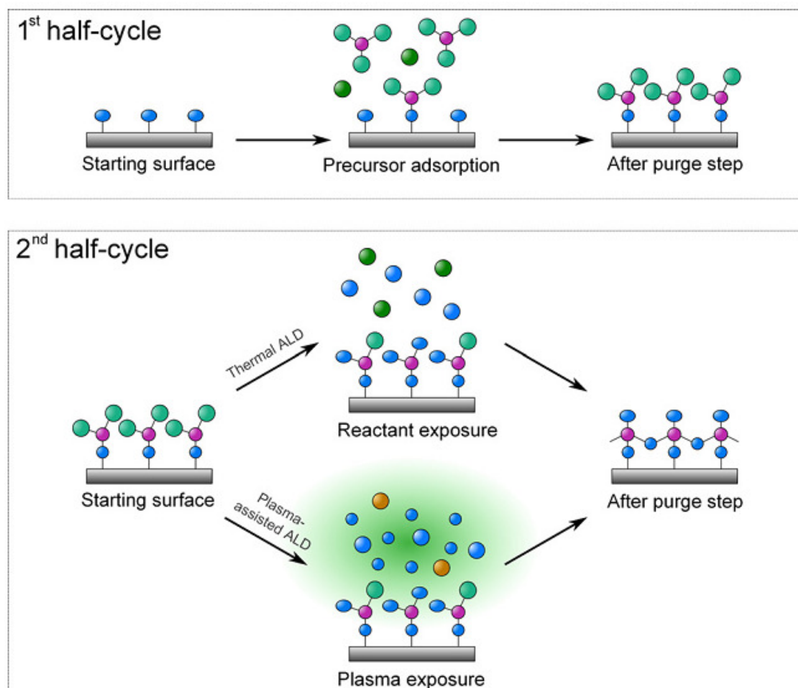

Figure 1.6 *Schematic representation of thermal and plasma-assisted ALD. The first half- cycle consists of an exposure to a precursor gas that is followed by a purge. In this half-cycle adsorption of precursor molecules takes place. In the second half-cycle the surface is exposed to a reactant gas or to species generated by a plasma. The second half-cycle is again finished by a purge. The two half-cycles together form the ALD cycle.*

ALD is a deposition technique that is rapidly gaining interest. The number of reported materials that are deposited by ALD is still growing. The available precursors are under constant development as well, in order to make them better and safer to use.

1.4 Project Goals

This chapter showed that (doped) ZnO is reported to be a promising candidate for many existing and novel applications. Furthermore, ALD seems to be a viable deposition method for ZnO. These conditions already led to many reports on the ALD of ZnO [20-27]. Most of these reports however, report on the thermal ALD of ZnO. Little work has been reported on plasma-assisted ALD of ZnO.

Besides reports on ALD of intrinsic ZnO, there are a lot of reports on the ALD of doped ZnO. Aluminium doping, for example, is of interest for tuning the material resistivity [28-41]. In all these reports *trimethyl-aluminium* (TMA) was used as the aluminium precursor.

TMA however, is pyrophoric and potentially dangerous to use in high-volume manufacturing applications. It is interesting to explore the possibilities of other aluminium precursors that are less pyrophoric. *Dimethyl-aluminium isoproxide* (DMAI) seems a viable alternative of TMA. Aluminium doping of ZnO with the use of DMAI was not yet been investigated. A comparison of TMA and DMAI as doping precursors is therefore interesting from both industrial and scientific viewpoints.

Based on these conditions and existing research, the following project goals were set:

- Develop both thermal and plasma-assisted ALD processes for ZnO. The ALD of ZnO is new for the PMP group. Only little literature on the plasma-assisted ALD of ZnO is currently available;
- Characterize the resulting material properties of intrinsic ZnO, both for thermal and plasma-assisted ALD, using specialized diagnostic techniques. Examples of the techniques used are spectroscopic ellipsometry, Rutherford backscattering spectroscopy and X-ray photoelectron spectroscopy;
- Develop ALD processes for aluminium-doped ZnO, using both TMA and DMAI as aluminium precursors. The ALD of aluminium-doped ZnO with TMA was described in the literature. The DMAI precursor however, is relatively new. This research will be the first attempt to use DMAI in the ALD of aluminium-doped ZnO;
- Use diagnostic techniques to compare the properties of TMA and DMAI as aluminium precursors for the ALD of aluminium doped ZnO.

1.5 Thesis Outline

This thesis consists two main parts. The first part elaborates on the process development and characterization of intrinsic ZnO and is described in Chapter 3. The second part elaborates on the ALD of aluminium doped ZnO, with different aluminium precursors. This part is described in Chapter 4. Prior to the two main parts, an explanation of deposition and special diagnostic techniques is given in Chapter 2.

Chapter 2

Deposition & Diagnostic Techniques

2.1 ALD Reactor

All depositions were carried out on an Oxford Instruments OpAL^{TM} reactor located in the ISO class 6 clean room in the NanoLab@TUe. The reactor is depicted in Figure 2.1. It is an open-load system, which features a remote-inductively-coupled plasma source. The reactor consists of a deposition chamber that is continuously pumped by a rotary vane pump. On top of the reaction chamber the plasma source is connected through a gate valve. The plasma source can deliver up to 300 W plasma power at 13.56 MHz and is controlled by an automated matching network. A substrate holder is located in the centre of the reaction chamber and can hold substrate sizes up to 200 mm. The substrate holder can be heated up to 400 ^{o}C. The chamber wall and gate valve temperature can be controlled separately. The wall and gate valve temperatures were chosen to be equal to the substrate temperature for all depositions. However, the wall and gate valve temperatures can only be set to temperatures up to 180 and 120 °C respectively. During deposition the typical pressure was between 50 – 500 mTorr.

Precursors are delivered into the process chamber by fast ALD valves from bubbler source pots that are situated in independently-heated modules, close to the deposition chamber. The delivery of the precursor can be either vapour-drawn or via bubbling of the precursor with ultra pure argon carrier gas. After precursor delivery the delivery lines are purged by the argon gas to remove remaining precursor. The gate valve can be purged separately. The precursor delivery lines from the module to the process chamber are heated 20 ^{o}C higher than the bubbler temperature, to prevent condensation in the delivery lines.

Two diagnostics ports are located outside the process chamber at 70° with respect to the substrate normal. These ports allow for in-situ spectroscopic ellipsometry measurements.

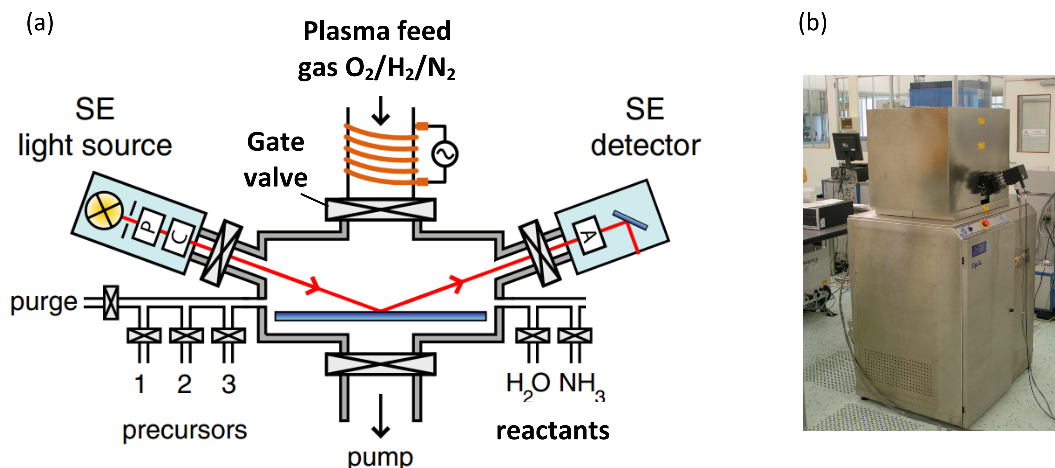

Figure 2.1 *Oxford Instruments OpAL™ ALD reactor. (a) Schematic representation (b) Photograph.*

2.2 Precursors

The precursor that was used for ZnO was Diethylzinc (DEZ), $Zn(C_2H_5)_2$. The precursor was contained in a stainless steel bubbler provided by Dockweiler Chemicals GmbH. The vapour pressure was 2 kPa at 20 ^{O}C, which is relatively high. Therefore the bubbler was not actively heated. No bubbling was needed during deposition. Table 2.1 shows a number of properties of DEZ.

The aluminium precursors that were used for aluminium doped ZnO will be described in Chapter 4. Appendix A contains an overview of all the precursors that were used, together with their properties.

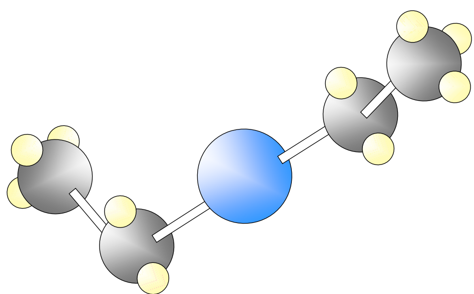

Figure 2.2 *Diethylzinc molecule. Blue = Zn, black = C, white = H.*

Table 2.1 *Properties of DEZ*

Precursor property	DEZ
Physical state (R.T.)	Liquid
Melting point	-28 ^{o}C
Boiling point	118 ^{o}C
Decomposition temperature	>200 ^{o}C
Vapour pressure	9 Torr at 15 ^{o}C
Pyrophoric	Yes

2.3 Spectroscopic Ellipsometry

Spectroscopic ellipsometry (SE) is a technique that is suitable to determine the thickness and optical properties of thin films [42]. It measures the change in polarization state of the light that is reflected from the sample surface. The change in polarization state, expressed in terms of amplitude ratio Ψ and phase angle Δ, is determined for a set of wavelengths in a specified photon energy range. The parameters of interest are subsequently deduced by matching an optical model with the obtained data, using ellipsometry software. SE can be used both in-situ and ex-situ the reactor chamber. The working principle is shown in Figure 2.3.

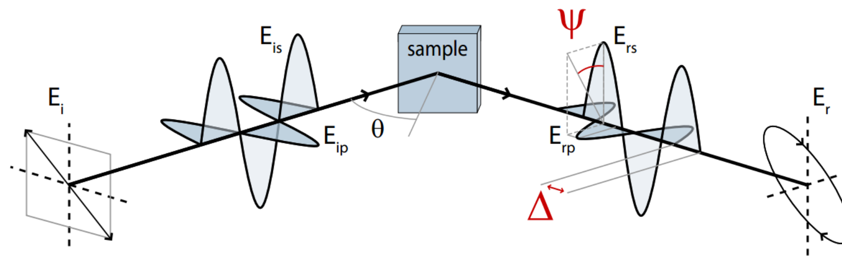

Figure 2.3 *The principle of spectroscopic ellipsometry. A polarized, incident wave interacts with the sample whereby the amplitude ratio Ψ and phase angle Δ change. The parameters of interest are subsequently deduced fitting the measured data to an optical model, using ellipsometry software*

The SE measurements were performed using a J.A. Woollam Co. Inc. M-2000D together with a XLS-100 light source (1.2-6.5 eV), or a M-2000F together with a FLS-300 Xe arc light source (1.2-5.0 eV). The data was analyzed using CompleteEASE ellipsometry analysis software. The thickness of the layers was found by matching the data with a Cauchy model to obtain the dielectric function [43]. This model is only valid in spectral regions where the layer shows no absorption. For ZnO this typically was between 1.2 and 3.0 eV. For all other SE measurements the dielectric function was determined by using a mathematical B-spline model with help of Jan Willem Weber and Valentino Longo. Transmittance was determined over the instrument's whole wavelength region by measuring the light intensity in a 'straight through' configuration. This corresponded to θ = 90 ^{o} in Figure 2.3.

2.4 Four-point Probe

Four-point probe (4pp) is a technique to determine the electrical resistivity of the samples. The 4pp setup consists of four evenly-spaced needles that are pressed on to the sample. This is shown in Figure 2.4. An electrical current is forced through the outer needles. The resulting voltage drop is measured over the two inner needles. For s>>t, the resistivity proved to be [9]:

$$\rho = \frac{\pi \cdot t}{\ln 2} \cdot \frac{V}{I} \tag{2.1}$$

Where ρ is the electrical resistivity, t the sample thickness, V the measured voltage and I the driving current.

The setup consisted of a Keithley 2400 SourceMeter and a Signaton S-301-6 probe. A home-built Labview program was used to control the Keithley. 100 current points were measured between the minimum and maximum current setting. The lowest possible current setting was 0.001 mA. The resistance was extracted from the slope of the resulting I-V curve. The resistivity was calculated from the resistance by formula (2.1). The resistivity of each sample was taken to be the average of five measurements on different sample positions.

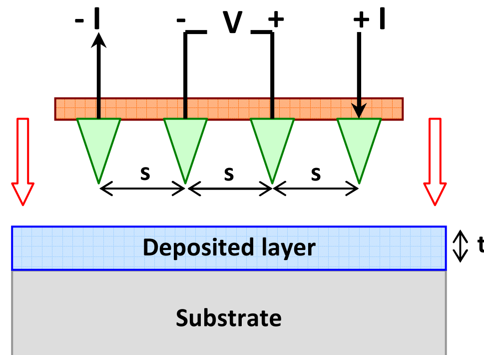

Figure 2.4 *Four-point probe technique. Four needles are pressed on to the sample. A current is forced through the outer needles. The resulting voltage is measured over the inner needles. The ratio between V and I is the resistance. This ratio can be converted into resistivity by formula (2.1).*

2.5 Hall System Measurements

A Hall system can be used to measure the electronic properties of the material. These properties are related to each other by [9]:

$$\rho = \frac{1}{q(n \cdot \mu_n + p \cdot \mu_p)} \tag{2.2}$$

Where ρ is the resistivity, q the elementary charge, n the free electron density, μ_n the free electron mobility, p the hole density and μ_p the hole mobility. Generally the material is either n-type meaning that $n >> p$, or p-type which means that $p >> n$. Therefore the formula can be rewritten as:

$$\rho \approx \frac{1}{q \cdot m \cdot \mu_m} \tag{2.3}$$

Where m is either n or p. With the Hall system, both the electronic resistivity ρ and free carrier density m are measured. The mobility μ_m is subsequently calculated by equation (2.3). The resistivity is measured by four probes in the van der Pauw configuration [9]. The free carrier concentration is determined by a Hall measurement [9]. The Hall measurement uses a magnetic field to create a Lorentz force on the moving charges in an electrical current. The Lorentz force drives the charges to one site of the material, creating a potential difference over the material. This potential difference can be measured and related to the charge density by:

$$m = \frac{I \cdot B}{q \cdot d \cdot V_H} \tag{2.4}$$

Where I is the electric current, B the magnetic field, d the thickness of the material and V_H the measured potential difference. The principle of the Hall measurement is shown in Figure 2.5.

The Hall system measurements were carried on a BioRad Hall system at Philips MiPlaza by Michiel Blauw from Holst Centre.

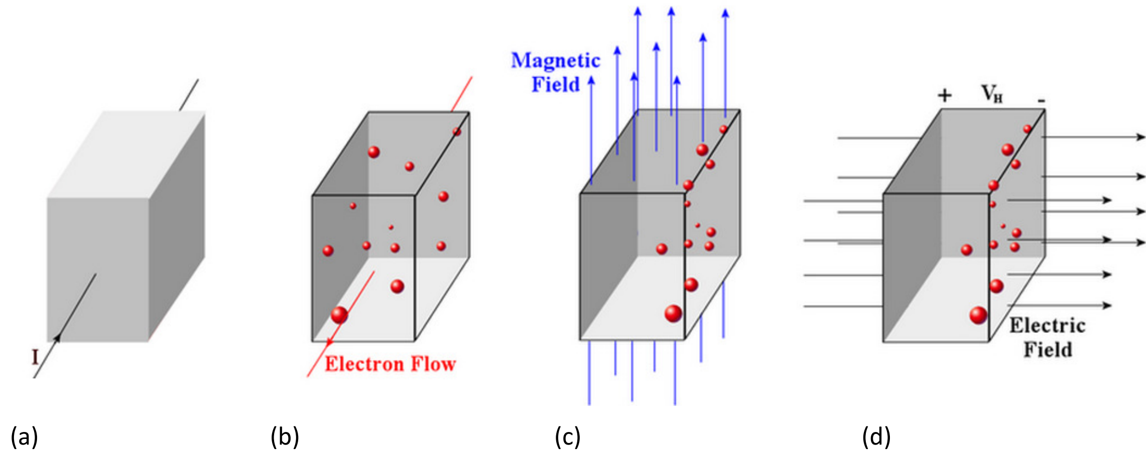

Figure 2.5 *Principle of Hall measurement to measure the charge density. (a) Shows the electrical current. (b) shows the electron flow of the current. (c) shows the electrons that accumulate during the interaction with the magnetic field. (d) shows the resulting potential difference that can be measured. The measured voltage is related to the charge carrier density by formula 2.4.*

2.6 Rutherford Backscattering Spectroscopy/Elastic Recoil Detection

Rutherford backscattering Spectroscopy (RBS) is a technique that can be used to determine material composition and the areal density of atoms (number of atoms/cm^2). From these properties also the mass density can be calculated when the thickness of the sample is known. A particle accelerator is used to target a high energy (1-2 MeV) beam of $^4He^{2+}$ ions, at the sample. These ions are subsequently scattered from the surface. A detector is placed under a specific angle and counts the number of scattered ions. The energy of these ions is measured as well. From the data, the mass and therefore the species of the target atom, as well as the target atom depth within the sample can be determined. The principle of the method is shown in Figure 2.6a.

Hydrogen atoms are too light and are recoiled instead of scattered. Therefore a second technique is used for the detection of H. This technique is *Elastic Recoil Detection* (ERD), which is carried out on the same apparatus as RBS. With ERD the incident ion beam is directed at a grazing angle to the sample. The detector is used to measure the recoiled H atoms. An additional 'stopper foil' is needed to prevent detection of scattered ions. The principle of ERD is shown in Figure 2.6b.

Both RBS and ERD measurements were carried out by Wim Arnold Bik of Acctec B.V. Acctec is located at the TU/e.

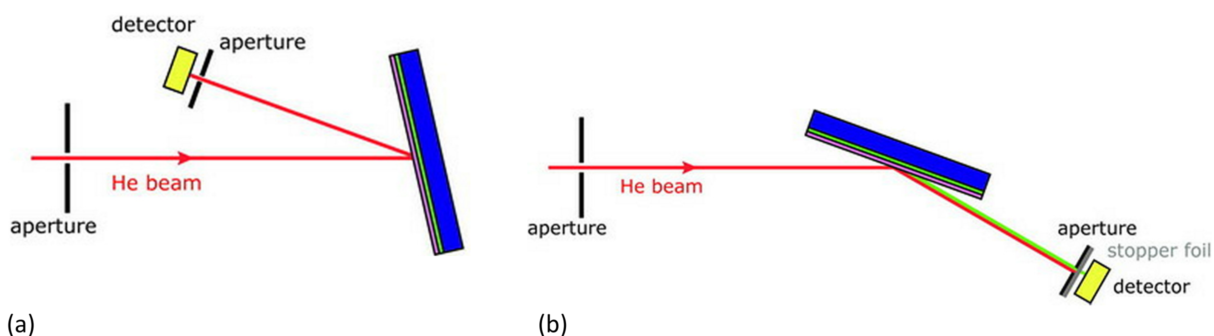

Figure 2.6 *(a) RBS setup. A high energy ion beam is targeted to the sample. A detector is placed under a fixed angle and counts the number of scattered ions. The energy of the scattered ions is also measured. From the data the species of the target atoms, as well as their depth within the sample can be determined. (b) ERD setup. A high energy ion beam is directed at a grazing angle to the sample. The detector is used to measure the recoiled H atoms. An additional 'stopper foil' is needed to prevent detection of scattered ions.*

2.7 X-ray Photoelectron Spectroscopy Study

X-ray photoelectron spectroscopy study (XPS) is a technique to measure the chemical composition, chemical state and electronic state of the material. An X-ray beam is targeted onto the sample, causing electrons to escape from the material. The kinetic energy of these electrons can be measured, from which the electron binding energy can be deduced. A XPS spectrum shows the electron counts as a function of binding energy, which is specific for each type of atom. Combining the technique with ion milling, allows for measuring depth profiles.

XPS measurements were carried out by Yizhi Wu in the NanoLab@TUe clean room. A Thermo Scientific K-Alpha system was used.

2.8 X-ray Diffraction

X-ray diffraction (XRD) is a technique that reveals information about the chemical and crystallographic structure of the material. In a crystalline material the crystal lattice is arranged so that the atoms form a series of parallel planes. These planes are separated from one another by a distance d. For any type of crystal, planes exist in a number of different orientations, each with a specific d-spacing. When a monochromatic X-ray beam with wavelength λ is projected onto a crystalline material at an angle θ, diffraction occurs only when the distance travelled by the rays reflected from successive

planes differs by a complete number *n* of wavelengths. This condition is called the Bragg law [44]:

$$n \cdot \lambda = 2 \cdot d \cdot \sin\theta \tag{2.5}$$

By varying the angle θ, the Bragg's law conditions are satisfied by different *d*-spacings in polycrystalline materials. Plotting the angular positions and intensities of the resultant diffracted peaks of radiation produces a pattern, which is characteristic of the sample.

XRD measurements were carried out by Wytze Keuning in the NanoLab@TUe clean room. A PANalytical X'Pert Pro MRD system was used.

Chapter 3

Process Development & Characterization of Intrinsic Zinc Oxide

This chapter describes the intrinsic ZnO ALD process development and characterization. The first section describes the ZnO process development. The second section elaborates on the material characterization.

3.1 Process Development

ALD process development requires finding the optimum step times of the four steps in an ALD cycle, for a specific substrate temperature. These four steps are precursor dosing, precursor purge, reactant dosing and reactant purge (see Figure 1.6). The step times should be minimized in order to get the shortest possible cycle time. The precursor and reactant step times must be long enough however, to ensure adsorption on all surface sites and hence an excellent film uniformity. The purge step times have to be long enough to remove excess precursor, reactant and reaction products. This is to avoid CVD-like reactions between precursor and reactant in the gas phase.

The minimum step times were determined by measuring the saturation curves. A saturation curve shows the growth per ALD cycle as a function of the step time of interest. A dose or purge time is in "saturation" when the growth per ALD cycle is independent of this dose/purge time. A standard ALD recipe was formed by choosing the minimum step times from the saturation regime in the saturation curves. This procedure was followed for both thermal and plasma-assisted ALD processes.

The *nucleation behaviour* is also a process characteristic. The initial film growth can be inhibited or accelerated. Because of this it can take a number of ALD cycles, before the thickness increases linearly with ALD cycles, as is the case for an "ideal" ALD process. A low number of substrate adsorption sites for instance, can inhibit initial growth. The nucleation behaviour of ZnO on silicon was studied in order to enhance accurate prediction of layer thickness during deposition.

3.1.1 Experimental Details of Process Development

Both thermal and plasma-assisted processes were developed at a substrate temperature of 150 °C. This temperature was chosen since the growth per cycle that was reported in the literature, showed to be maximum at this point, as described in section 3.2.2.

For the thermal process H_2O vapour was used as reactant. During operation, material is deposited everywhere in the reactor, including the gate valve, which is a moving part as described in section 2.1. When operating the gate valve, the deposited material risks coming off in the form of flakes. Therefore, the gate valve is purged with a 150 sccm Ar flow during precursor and H_2O dosing, to prevent local material deposition. The complete thermal ALD recipe is described in Table 3.1 and also in Appendix B.

The plasma-assisted process was less straightforward than the thermal. A 200 W O_2 plasma was used as reactant. The gate valve was again purged with Ar to prevent local material deposition that could cause flakes. The Ar flow was maintained between 70 and 100 sccm. The exact flow value depended on the total pressure, which was kept below 300 mTorr.

The plasma-assisted process required an additional N_2 flow of 100 sccm through the *inductively-coupled plasma* (ICP) source as well. This flow was necessary during the DEZ dose in order to prevent material deposition on the ICP source. Conducting material like ZnO can interfere with the ICP source operation by damping the radiation that is applied to the O_2 gas during the plasma step. N_2 instead of O_2 was chosen for this purpose since N_2 does not react with DEZ, while O_2 does. The N_2 and O_2 gases use the same line however. As a consequence, a 5 second N_2 removal/O_2 build up step was required after the precursor purge. This 5 second N_2 removal/O_2 build up prolonged the plasma-assisted recipe and is therefore a drawback. Future plans are to install a separate Ar line into the ICP-source. Ar is not reactive to DEZ or O_2 and a continuous Ar flow during all steps, will replace the necessary N_2 flow. Table 3.2 describes the plasma-assisted recipe. This recipe is also shown in Appendix B.

Saturation curves were measured by determining the GPC as function of the step time. For this, the step time of interest was varied while the other step times were taken to be long enough to ensure they were in saturation. 200 cycles were deposited on a silicon wafer while the thickness was measured every 10 cycles by in-situ SE. This resulted in graphs of thickness versus ALD cycles. The slope of the linear part of the graph was then taken to be the *growth per cycle* (GPC). The GPC was based on the linear part of the graph only, to exclude possible nucleation effects.

The nucleation behaviour was measured by depositing 100 ALD cycles on a silicon wafer and measuring the thickness after each ALD cycle by in-situ SE. During deposition the optimum settings were used that followed from the saturation curves.

Table 3.1 *Recipe of the thermal ALD process at 150 ^oC deposition temperature*

	DEZ dose 30 ms	DEZ purge 5 s	H_2O dose 20 ms	H_2O purge 6 s
DEZ	on	off	off	off
H_2O	0	0	1	0
Ar gate valve (sccm)	150	0	150	0
Ar through DEZ (sccm)	0	150	0	0
Ar through H_2O (sccm)	0	0	0	150
gate valve	0	0	0	0

Table 3.2 *Recipe of the plasma-assisted ALD process at 150 ^oC deposition temperature*

	DEZ dose 30 ms	DEZ purge 1 s	Remove N_2 + O_2 build up 5 s	O_2 plasma dose 4 s	O_2 plasma purge 6 s
DEZ	on	off	off	off	off
O_2 (sccm)	0	0	50	50	0
N_2 (sccm)	100	100	0	0	100
Ar gate valve (sccm)	70	0	100	100	70
Ar through DEZ (sccm)	0	100	0	0	0
Plasma power (W)	0	0	0	200	0
Plasma source mode	HOLD	HOLD	HOLD	HOLD	HOLD
gate valve	1	1	1	1	1

3.1.2 Results & Discussion of Process Development

Figures 3.1 and 3.2 show the saturation curves of the thermal and plasma-assisted ALD process respectively. The red lines act as guides to the eye while the lines of the H_2O dosing are mathematical fits.

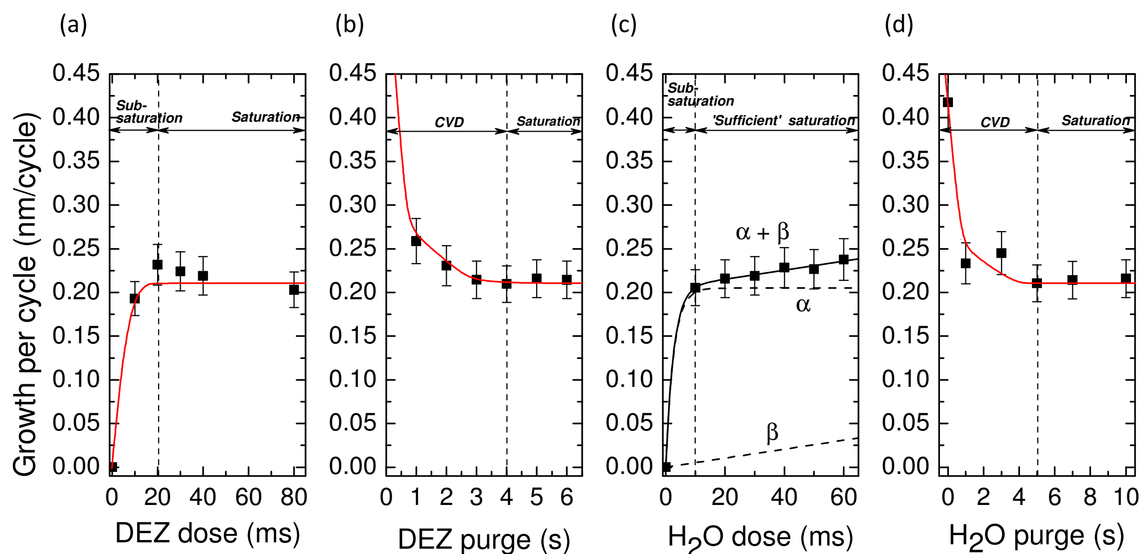

Figure 3.1 *Thermal ALD saturation curves at a substrate temperature of 150 °C. The red lines act as a guide to the eye' while the reactant dosing line is a mathematical fit. This fit consists of an exponential contribution (α) superposed with a linear contribution (β). These two contributions suggest that two processes play a role.*

The thermal process saturation curves in Figure 3.1a,b,d show typical ALD behaviour. That is, a constant GPC in the saturation regime, combined with a sub-saturation regime for lower dosing values in Figure 3.1a,c and a CVD-like regime for lower purging values in Figures 3.1b,d. The reactant dosing curve in Figure 3.1c shows soft saturation. This means that the GPC keeps increasing with increasing reactant dosing times. The curve was fitted by superposing an exponential (α) and a linear fitting function (β). These two functions suggest two simultaneously occurring processes. The first process is the typical ALD process that contributes the exponential behaviour of function (α). The second process is some sort of additional growth that is linear with H_2O exposure, given by function (β). This additional growth was attributed to an increased OH group density on the film surface that results from H_2O overdosing. This was proposed by Matero et al., who experienced a similar effect with the thermal ALD of Al_2O_3, using *trimethyl-aluminium* (TMA) and H_2O [45]. This explanation was acknowledged by Henn-Lecordier et al. and their experiments led to a more detailed description of the mechanism [46]. In this description the bipolar nature of H_2O causes additional H_2O adsorption to the surface, depending on H_2O dosing time. This excess H_2O could not be completely removed by the subsequent H_2O purge step. TMA shows high reactivity with H_2O and is therefore likely to react with the excess H_2O, during the following precursor dose step. The reactions between TMA and excess H_2O then cause additional growth. Henn-Lecordier et al. described this mechanism for growth of Al_2O_3 by using TMA as precursor. The same mechanism might be present in the case of DEZ.

The curves show that saturation occurs at approximately 20 ms precursor dose, 4 s precursor purge, 10 ms H_2O dose and 5 s H_2O purge. A safety margin was incorporated in the final recipe so the chosen values were: 30 ms precursor dose, 5 s precursor purge, 20 ms reactant dose and 6 s reactant purge. The GPC was found to be 0.21 nm/cycle. Table 3.1 describes the thermal ALD process with all relevant reactor settings. The dosing times that were reported in the literature varied over a wide range between 20 ms and 4 s for the DEZ dose and between 15 ms and 2.5 s for the H_2O dose [20-27]. Every ALD reactor has very specific dosing times, which makes comparison to the literature very difficult.

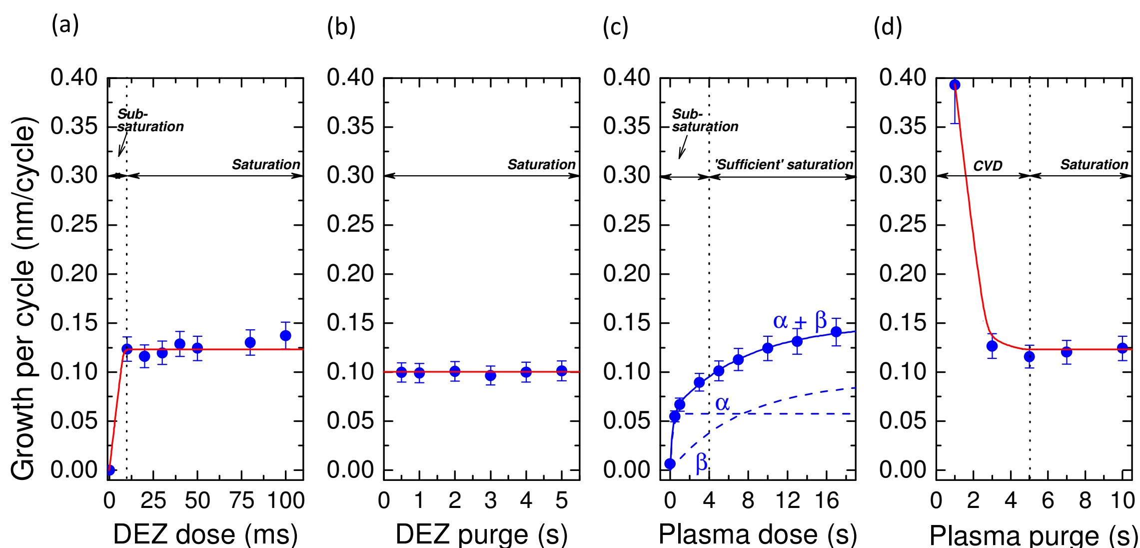

Figure 3.2 *Plasma-assisted ALD saturation curves at a substrate temperature of 150 °C. The red lines act as a guide to the eye while the reactant dosing line is a mathematical fit. This fit consists of two superposed exponential contributions (α) and (β). Note that de GPC of (b) is lower than that of (a) and (d). The reason is that (b) was measured with a plasma dose of 5 s while (a) and (d) were measured with a plasma dose of 10 s. These differences however, had no influence on the final saturation settings that were chosen, since a 4 s plasma dose was chosen in the end.*

The plasma-assisted process saturation curves in Figures 3.2a,b,d, show typical ALD behaviour. Note that the precursor purge time in Figure 3.2b can be arbitrarily low. This is caused by the preceding 5 second N_2 removal/O_2 build up step, which already acts as effective purge. Table 3.2 makes this more apparent. The reactant dosing curve in Figure 3.2c shows soft saturation. The process is not even saturated after 16 s which is an unpractically long step time.

The initial explanation was that the plasma conditions were not optimally chosen. There could have been insufficient reactive species for instance. This could be caused either by a plasma power, or an O_2 flow that was chosen too low. The plasma pressure could also

be too high, causing a high recombination rate and subsequently cause loss of reactive species that normally attribute to the deposition process. Finally, the continuous Ar flow could interfere with the plasma as well. A couple of tests were carried out to investigate these possibilities:

1. Changing the plasma power from 200 W to 300 W;
2. Increasing the O_2 flow during the plasma step from 50 sccm to 80 sccm. The total pressure was maintained constant by simultaneously reducing the Ar flow from 100 sccm to 70 sccm;
3. Reducing the total pressure during the plasma step by reducing the O_2 flow from 50 sccm to 30 sccm and the Ar flow from 100 sccm to 50 sccm;
4. Turning the Ar flow off during all dosing steps.

None of these tests had any influence on the measured GPC and so the initial explanation was rejected.

Observing the reactant dosing curve more closely showed that the function could be fitted by a double exponential function with two time constants (α) and (β):

$$y = y_0 + A_1(1 - e^{-t/\alpha}) + A_2(1 - e^{-t/\beta}) \tag{3.1}$$

These two time constants suggested that two processes play a role. First a process with a short time constant of 0.3 s, component (α) and second a process with a long time constant of 7 s, which was component (β). The origin of these two contributions is not yet established. However, there are two possible explanations for this behaviour. The first explanation is that a thermal growth component was present beside the plasma-assisted growth component. This thermal component could be caused by reactions between O_2 molecules and available OH surface groups or surface ethyl groups from the DEZ. This possibility can be tested by running the ALD cycles with the plasma power turned off. A positive GPC value will still be measured in case this explanation is true. A second possibility is additional O incorporation with increasing plasma dose. This additional O may cause an increased GPC value. This possibility can be tested by depositing samples with different plasma doses and subsequently measure the O content by RBS or XPS.

The curves show that saturation occurs after approximately 10 ms precursor dose, 0 s precursor purge and 5 s reactant purge. A safety margin was incorporated in the final recipe so the chosen values were: 30 ms precursor dose, 1 s precursor purge and 6 s reactant purge. In order to determine the plasma dose, two 4 inch samples of approximately 58 nm were deposited with 4 s and 12 s plasma dose. These samples were compared in terms of dielectric function, non-uniformity and resistivity. The

dielectric functions and non-uniformity proved to be similar. The measured resistivity of the 4 s plasma dose was a factor 10 lower than that of the 12 s. Higher plasma dosing may lead to more O incorporation, leading to higher resistivity as described in section 1.2. Combined with the desire to get the shortest possible recipe, this led to the choice to proceed with a 4 s plasma dose.

The GPC for the chosen settings was 0.09 nm/cycle, as can be seen in Figure 3.2c. Note that this is far into the saturation regime of the first exponential fit function (α). A higher plasma dosing time would lead only to moderate increase in GPC, according to fit function (β). Also note that the GPC in the curves of 3.2a,b,d, are higher than 0.09 nm/cycle. The reason is that these curves were measured with higher plasma doses of 5 s in Figure 3.2b and 10 s in Figure 3.2a,d. These alternative settings plasma dosing settings however, did not influence the points at which the remaining saturation regimes started.

The graphs in Figure 3.3 show the nucleation behaviour of both ALD processes. To obtain these graphs from the measured data, the SE model parameters were kept constant and the film thickness was fitted backwards.

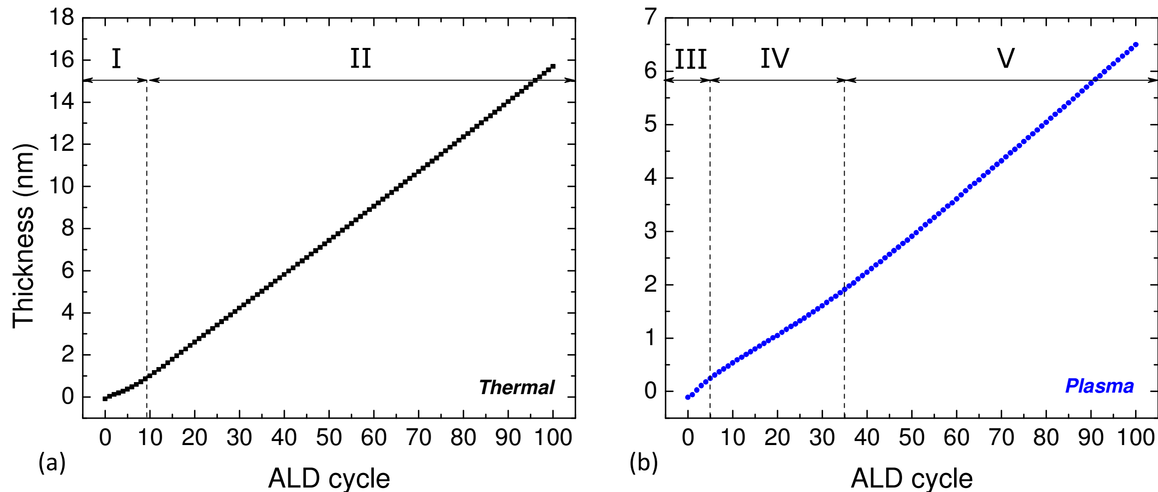

Figure 3.3 *Graphs of thickness versus ALD cycle on a silicon substrate at 150 °C. (a) Thermal process (b) Plasma-assisted process*

Figure 3.3a shows inhibited growth of the thermal process during approximately the first 10 cycles. This is denoted as region I. The GPC becomes linear after approximately 10 cycles. This is denoted by region II.

The graph of the plasma-assisted process in Figure 3.3b shows three different regions. First there is region III with accelerated growth within approximately the first 6 cycles. Second of all, there is region IV where the graph shows inhibited growth. This is approximately between 6 and 32 cycles. Finally, there is region V above 32 cycles. In this region the graph shows linear growth.

The particular shape of the plasma-assisted nucleation graph could be explained qualitatively by a model that was proposed by Nilsen et al., which is also known as "Volmer-Weber growth" [47]. This model is explained by Figure 3.4. The basic assumption was that the difference in number of adsorption sites, on the substrate and the film, leads to initial island growth. The initial stage of island growth is depicted in Figures 3.4a,b. The dark orange lines represent the surface area on which material will be deposited in the next ALD cycle. The island size and surface area both increase with ALD cycles. This means that the amount of material that will be deposited during the next ALD cycle, which is related to the GPC value, also grows with ALD cycles. This corresponds to the accelerated growth behaviour of region III in Figure 3.3b.

At a certain point, the situation of Figure 3.4c is reached. The islands have grown to a size where they start to coalesce. Figure 3.4d shows that further ALD cycles result in a transition between island and flat surface growth. The surface area, on which material can be deposited, is reduced with ALD cycles. This behaviour corresponds to the inhibited growth of region IV in Figure 3.3b. After growing even further, the flat surface growth of Figure 3.4e is finally reached. Here the size of the surface area is constant with ALD cycles. This corresponds to the linear growth of region V in Figure 3.3b.

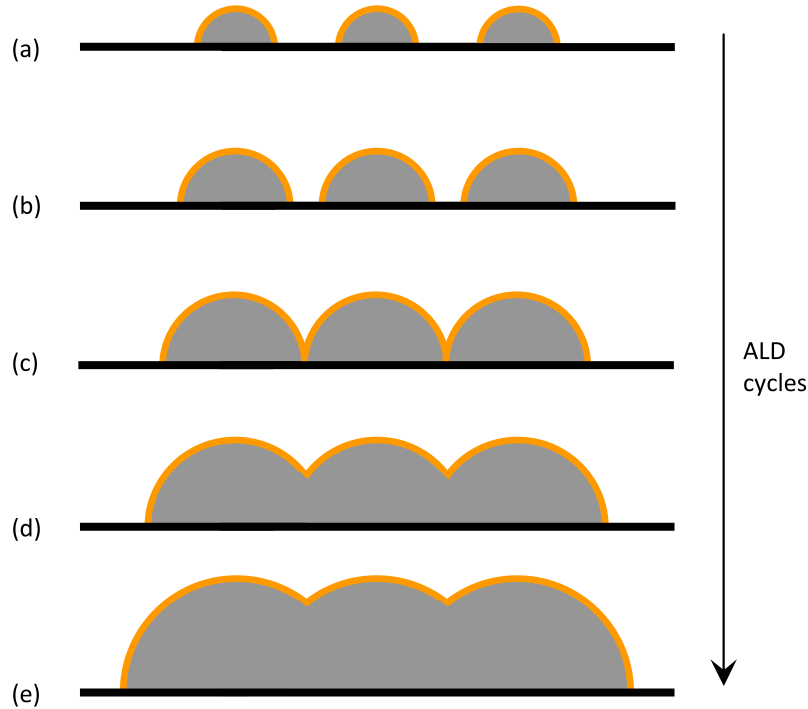

Figure 3.4 *Schematic representation of the island growth model that was proposed by Nilsen at al. The model shows the island size as a function of ALD cycles. The amount of material that will be deposited in a following ALD cycle is proportional to the island area, which is shown by orange lines. (a) + (b) show the initial stage of island growth. The surface area increases with increasing island size. (c) shows islands start to coalesce and the surface area reached its maximum value. (d) shows the transition between islands and flat layer. The surface area decreases with ALD cycles. (e) shows the final growth stage. The flat surface. Surface area is constant with ALD cycles*

The Nilsen model helps to understand why the plasma-assisted nucleation curve has the particular shape consisting of three regions in Figure 3.3b. The shape of the thermal nucleation curve however, could be explained by the model as well. Note that the thermal GPC is higher than the plasma-assisted GPC. This causes the flat surface state of Figure 3.4e to be reached much faster. As a consequence, the region of inhibited growth would become less apparent in the thermal nucleation graph of Figure 3.3a.

The thermal and plasma-assisted processes showed nucleation behaviour on a silicon substrate only within the first 10 and 35 cycles respectively. During nucleation the GPC differed slightly from the GPC after nucleation. All intrinsic ZnO layers that were deposited in the thesis work had a minimum thickness of approximately 40 nm. This corresponds to depositions of approximately 191 and 445 ALD cycles for the thermal and plasma-assisted processes, respectively. This means that nucleation behaviour had only a moderate effect on total layer thickness. The GPC values found in the saturation curves could therefore be considered accurate for thickness prediction of samples.

3.2 Intrinsic Zinc Oxide Material Characterization

After developing the thermal and plasma-assisted ALD processes of ZnO, the following properties of the material grown by these processes were investigated:

- GPC as a function of deposition temperature. This information provided the temperature regime in which the processes show sufficient growth and therefore could be efficiently applied;
- Material composition as function of deposition temperature, as measured by RBS/ERD;
- The *non-uniformity*. This is a measure of the thickness distribution within deposited layers. A low non-uniformity means that saturation conditions are met over the whole substrate, which is desirable;
- Electrical resistivity as function of deposition temperature. This is an important property regarding electronic applications;
- Transmittance as function of deposition temperature. Transmittance is important for TCO applications as described in Chapter 1;
- Optical band gap as function of deposition temperature. Optical band gap is also important for TCO applications;
- Crystalinity as function of deposition temperature;

The first sub-section provides the experimental details of depositions and measurements that were performed to determine the material properties. Further sub-sections elaborate on the results. The results were compared to literature values when possible.

3.2.1 Experimental Details of Intrinsic Zinc Oxide Characterization

For determining the non-uniformity, 400 and 850 cycles were deposited with a thermal and plasma-assisted ALD process respectively. These depositions were carried out in saturation conditions on an 8 inch silicon wafer. The substrate temperature was 150 ^{O}C. The thickness of the deposited layers was measured on a grid of 28 points by ex-situ SE. The non-uniformity was then calculated by [48]:

$$non-uniformity = \frac{d_{\max} - d_{\min}}{2 \cdot d_{average}} \cdot 100\% \qquad (3.2)$$

Were d_{max}, d_{min} and $d_{average}$ are the maximum, minimum and average measured thicknesses respectively.

The remaining properties were determined with three temperature series:

1. In the first temperature series a constant number of ALD cycles were deposited on silicon. The substrate temperature was varied between 50 ^oC and 400 ^oC, in steps of 50 ^oC. The material thickness was measured after deposition by ex-situ SE. Dividing the total thickness by the number of cycles gave the process growth per cycle as a function of temperature. Nucleation effects were neglected as justified earlier.

   250 and 550 ALD cycles were used for the thermal and plasma-assisted process respectively. The processes were assumed to be in saturation for each chosen substrate temperature. To ensure this, the precursor dosing times were prolonged to 50 and 40 ms for the thermal and plasma-assisted processes respectively. Reactant dosing and purge times were kept the same as in the standard recipes since they were already chosen with a relatively wide safety margin.

2. In a second temperature series, ZnO layers were deposited with a constant thickness of approximately 40 nm. Prolonged precursor dosing of 40 ms was used for both processes again to ensure saturation behaviour at all temperatures. Substrate temperatures were varied between 50 ^oC and 400 ^oC, in steps of 50 ^oC. Depositions were carried out on both silicon and glass substrates. The material thickness and ε_2 were determined by ex-situ SE from the silicon substrate samples. ε_2 is the complex part of the dielectric function. Ex-situ SE and *four-point probe* (4pp) were used to measure the transmittance and electrical resistivity respectively, from the glass substrate samples. The electrical resistivities were measured within 1 hour after deposition to exclude aging effects. The material thickness on the silicon substrates was assumed to be similar to that of the glass substrates. This was checked for one sample and found to be true.
3. In a third temperature series approximately 75 nm thick ZnO layers were deposited on silicon substrates. Prolonged precursor dosing of 50 ms for the thermal and 40 ms for the plasma-assisted processes were used again. The substrate temperatures were 100 ^oC, 200 ^oC and 300 ^oC. The material composition and crystalinity were measured by RBS/ERD and XRD respectively. ERD was only performed on the thermal process samples.

3.2.2 Growth per Cycle as a Function of Deposition Temperature

Figure 3.5 shows the GPC as a function of deposition temperature. Figure 3.5a contains the measured values for both. Figure 3.5b contains literature values for both processes. Note that the all literature values were measured on different types of ALD reactors, under different conditions. Only the values provided by Oxford Instruments were coming from a similar OpAL^{TM} reactor. These data points are marked by orange borders in Figure 3.5b.

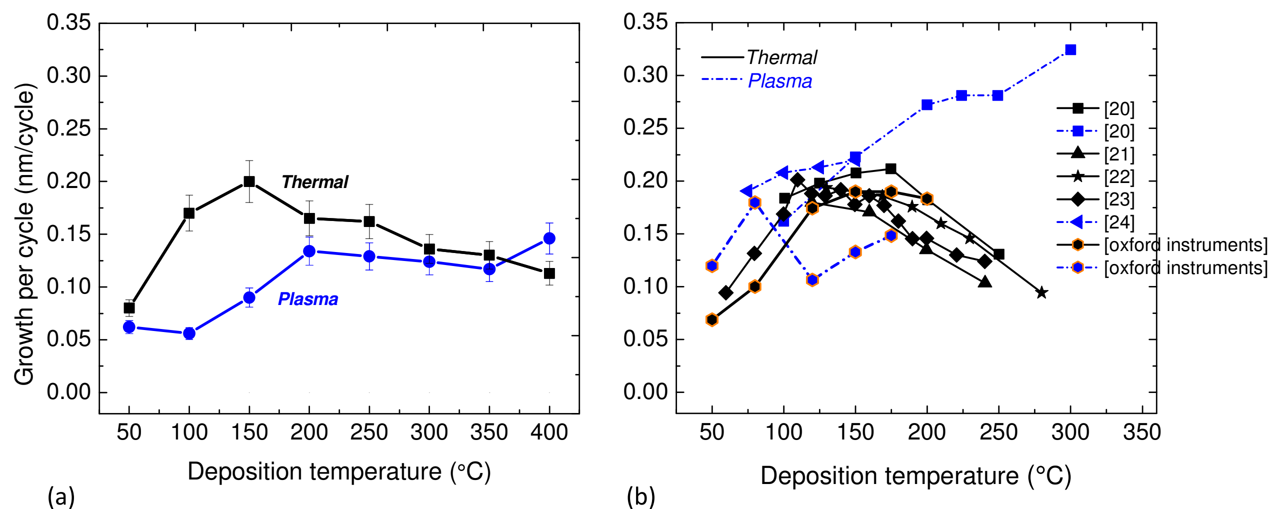

Figure 3.5 *Growth per cycle as a function of deposition temperature (a) Data obtained in this work. (b) Literature data. From the literature data only the Oxford Instruments points were coming from a similar OpAL™ reactor. These points are represented with an additional orange border*

The thermal process curve in Figure 3.5a increases between 50 and 150 °C. The GPC seems to reach a maximum value of approximately 0.21 nm/cycle at 150 °C. Above approximately 150 °C, the GPC gradually decreases with increasing deposition temperature.

The thermal literature curves in Figure 3.5b are consistent with each other and with the measurements. The curves show an increasing GPC between approximately 50 and 100 °C. In this region there may be insufficient thermal energy for chemical reactions to occur [17,18,49]. Between approximately 100 and 175 °C, the GPC is more or less constant with values of 0.17-0.22 nm/cycle. This is the optimal temperature region for the process with respect to GPC. In ALD literature this region is often denoted by *temperature* or *process window* [17,18,49]. At temperatures higher than 175 °C the GPC decreases with increasing deposition temperature. The higher thermal energies in this region may cause desorption of species that result in a lower GPC [17,18,49].

The plasma-assisted process curve in Figure 3.5a starts with a more or less constant GPC of approximately 0.06 nm/cycle, at deposition temperatures of 50 and 100 °C. This region was again associated with insufficient thermal energy for the reactions to take place. The GPC increases between 100 and 200 °C, where a maximum value of approximately 0.13 nm/cycle is reached at 200 °C. At temperatures higher than 200 °C the GPC seems to decrease with increasing deposition temperature. This region was appointed to be some sort of temperature window. At deposition temperatures above 350 °C the GPC starts increasing again. This might be due to thermal decomposition of the precursor, that causes CVD-like growth when decomposition products were exposed to the O_2 plasma [17,18,49].

Figure 3.5b contains three plasma-assisted literature curves. These curves are less consistent with each other and with the measurements. The curve measured by Kim et al. [20], increases over the whole temperature range and ends with a very high GPC of approximately 0.33 nm/cycle. There is no clear temperature window. Thermal decomposition could already be present at relatively low temperatures in the reactor that was used by Kim et al. Another reason could be that the purges were not taken long enough. This would explain the steep increasing curve. The second curve was measured by Park et al. [24]. This curve is increasing with temperature and shows a GPC between approximately 0.19 and 0.22 nm/cycle. No data points are available for temperatures above 150 °C. Finally, there is the curve provided by Oxford Instruments. This curve is not consistent with the measured data between 50 and 125 °C. In this region the GPC that was found by Oxford instruments, varies between approximately 0.11 and 0.18 nm/cycle. The measured values in this range where approximately constant with 0.06 nm/cycle. At temperatures above 125 °C the two curves become more consistent with each other. They show the same trend where the Oxford Instruments points are slightly higher by a constant value of approximately 0.03 nm/cycle. The exact shape of the entire Oxford Instruments curve can not easily be explained.

As conclusion of this experiment the thermal process temperature window was estimated to lie between deposition temperatures of 100 and 350 °C. For the plasma-assisted process the temperature window was estimated to lie between 200 and 350 °C. The thermal process showed a higher GPC than the plasma-assisted process in general. In terms of GPC and temperature window the thermal process seemed to be preferable above the plasma-assisted process.

3.2.3 Material Properties Measured by RBS/ERD

Figure 3.6 contains the graphs that were measured by RBS for both processes. The graphs show stochiometry, deposited atoms per cycle and mass density. ERD was only performed on the thermal process samples. This gave the H content of the sample that Figure 3.6d represents.

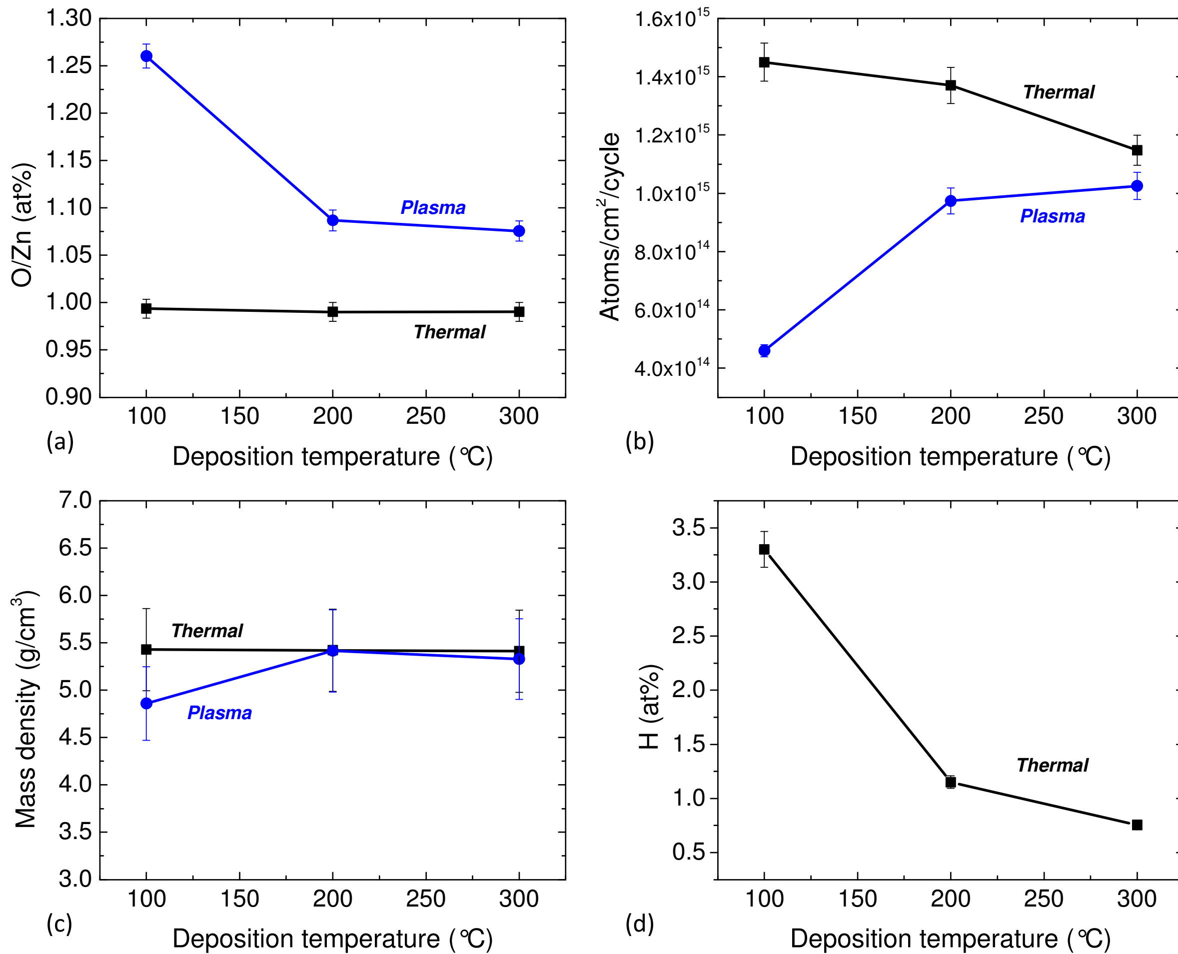

Figure 3.6 *Material properties measured by RBS/ERD as function of deposition temperature (a) O/Zn atomic ratio (b) Deposited atoms per cycle (c) Mass density (d) Atomic H content (thermal process only).*

Figure 3.6a shows the atomic O/Zn ratio as function of deposition temperature. For the thermal process this ratio was approximately 1 for all deposition temperatures. For the plasma-assisted process the value started at 1.25 for a deposition temperature of 100 °C, and decreased to a value of approximately 1.08 for both 200 and 300 °C. On average the thermal process contained the least O in the film. This was probably caused by the higher reactivity of the O species in a plasma, compared to H_2O vapour. Figure 3.6c shows that the thermal and plasma-assisted processes exhibited similar mass densities of approximately 5.5 g/cm^3. Figure 3.10d shows the H content as function of the deposition temperature for the thermal process. The graph shows that the H content decreased with increasing deposition temperature. Figure 3.8a it will be shown that the resistivity increased with increasing temperature. These findings are consistent with the concept of H acting as shallow donor as described in Chapter 1.

3.2.4 Non-uniformity

Figure 3.7 shows the non-uniformity measurement results. The thermal process showed a non-uniformity value of 3.3 %. This was considered to be a decent value since typical values lie between 0.3 and 4 % on 300 mm wafers [50]. The plasma-assisted process showed a value of 22.3 % which was considered to be very high.

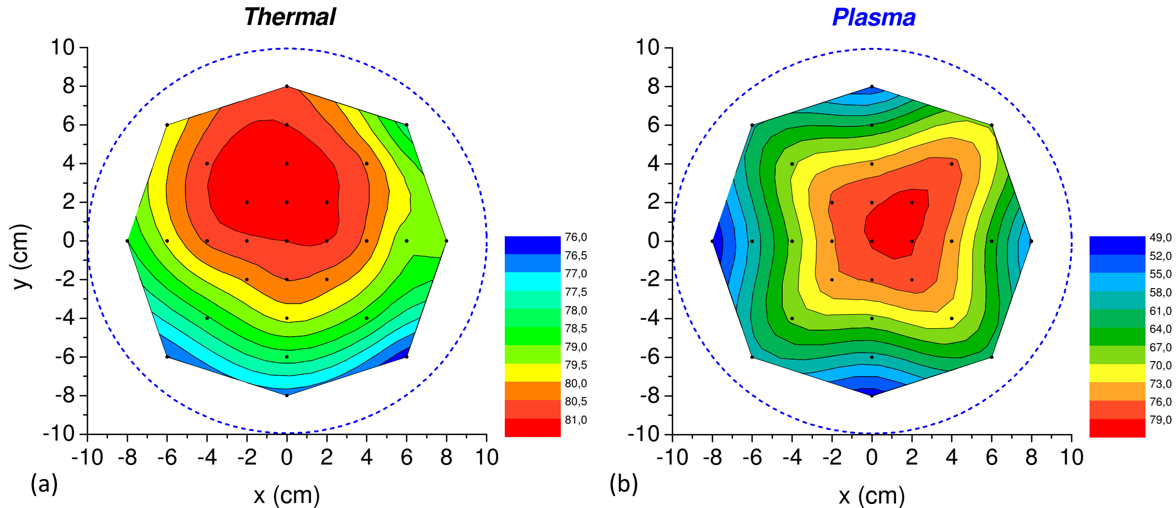

Figure 3.7 *Graphical representation of non-uniformity of (a) the thermal process and (b) the plasma-assisted process. The thickness was determined by ex-situ SE on 28 points of an 8 inch wafer. The colored planes are a two dimensional interpolation between these measured points. The layers were deposited at 150 °C.*

There are several important reasons that could cause non-uniformity [50]:

1. Overlapping precursor dosing steps can cause CVD-like reactions that locally produce increased thickness. This overlapping is the consequence of inadequate purging;
2. Precursor doses that are too short can cause the precursor to react completely in some area of the substrate causing local growth only;
3. A substrate temperature gradient can cause a gradient in GPC. Locally high substrate temperatures can cause precursor decomposition resulting in local CVD-like reactions;
4. A non-uniform precursor or reactant gas distribution can result in areas where saturation conditions are not met, causing limited growth within these areas;
5. Downstream reaction by-products can block active surface sites preventing further ALD reactions.

In the following, the possible causes of non-uniformity will be considered for the plasma-assisted process. Firstly, the purge times were chosen with a safety margin of a

couple of seconds within the saturation regime. Second of all, there was a 5 s N_2 build up step between precursor and plasma dose, as Table 3.2 shows. This means that reason 1 is unlikely to occur. Reason 2 is more likely to occur. Saturation curve 3.2c showed soft saturation of the plasma dose. In the end, a 4 s plasma dose was chosen that was based on a reasonable GPC that was only evaluated in the middle of the substrate. The time constants α and β of the fitting functions in Figure 3.2c, might however be dependent of position on the substrate. The mechanism causing the soft saturation can therefore possibly be position dependent, causing the GPC to vary with position. Reason 3 is unlikely since this would cause a similar non-uniformity in the thermal process. Reason 4 can possibly occur. During the reactant dose there was an Ar purge through the fill line as Table 3.2 shows. This purge is known to have no influence on the GPC in the middle of the substrate. However, it may have somehow influenced the plasma density, and thus the GPC, on other places on the substrate. Note however, that similar purges during the plasma-assisted Al_2O_3 process have no strong influence on the non-uniformity. Therefore reason 4 was finally rejected. Reason 5 is possible to occur as well. The exact reaction mechanism of the plasma-assisted process is not studied yet. Some reaction products might cause the blocking of surface sites. Note however, that one would expect this phenomenon more easily to happen in a flow-type reactor.

Based on non-uniformity the thermal process is preferable in general. The plasma-assisted process needs further development before it exhibits the typical advantage of low non-uniformity that ALD potentially has to offer. Non-uniformity issues are the possible reason that little literature is available on plasma-assisted ALD of ZnO.

3.2.5 Electrical Resistivity

Figure 3.8a shows the measured resistivity as a function of deposition temperature. The error bars are not clearly visible on the graph's logarithmic scale. This is why the uncertainty is also separately plotted in Figure 3.8b. Each resistivity value is the average of 5 four-point probe measurements on a sample. The standard deviation in these values is taken to be a measure of uncertainty. The solid lines in Figure 3.8b act as guide to the eye.

Figure 3.9 contains the material electrical properties that are found in the literature. Besides resistivity in Figure 3.9a, they comprise carrier concentration in Figure 3.9b and electron mobility in Figure 3.9c. These quantities are related to each other by the following formula [9]:

$$\rho = \frac{1}{q(n \cdot \mu_n + p \cdot \mu_p)} \tag{3.3}$$

Where ρ is the resistivity, q the elementary charge, n the free electron density, μ_n the free electron mobility, p the hole density and μ_p the hole mobility. ZnO is a n-type material. This means that $n >> p$. Therefore the formula can be written as:

$$\rho \approx \frac{1}{q \cdot n \cdot \mu_n} \tag{3.4}$$

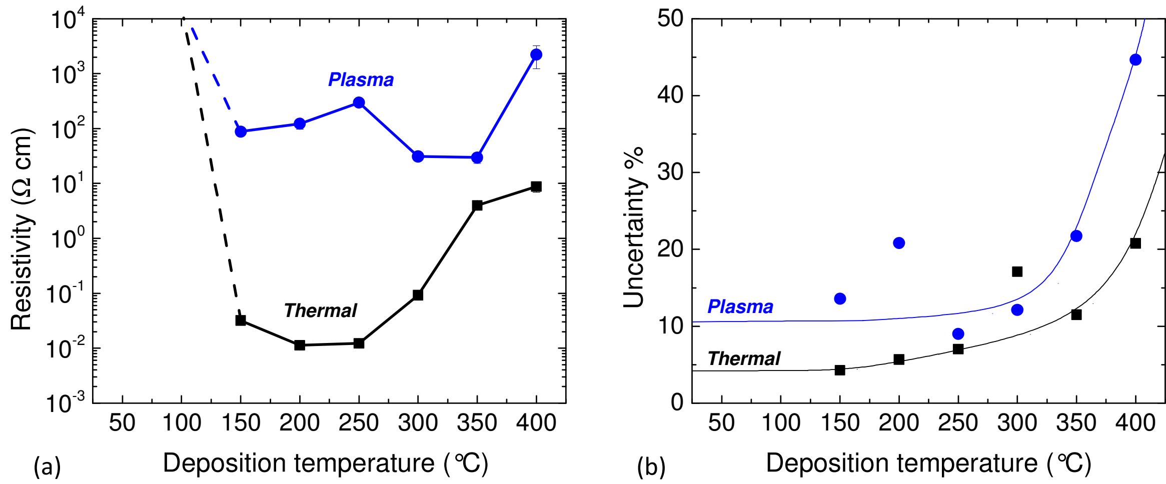

Figure 3.8 *Electrical resistivity for layers of approximately 40 nm, as a function of deposition temperature (a) Data obtained in this work (b) Separately plotted uncertainty values*

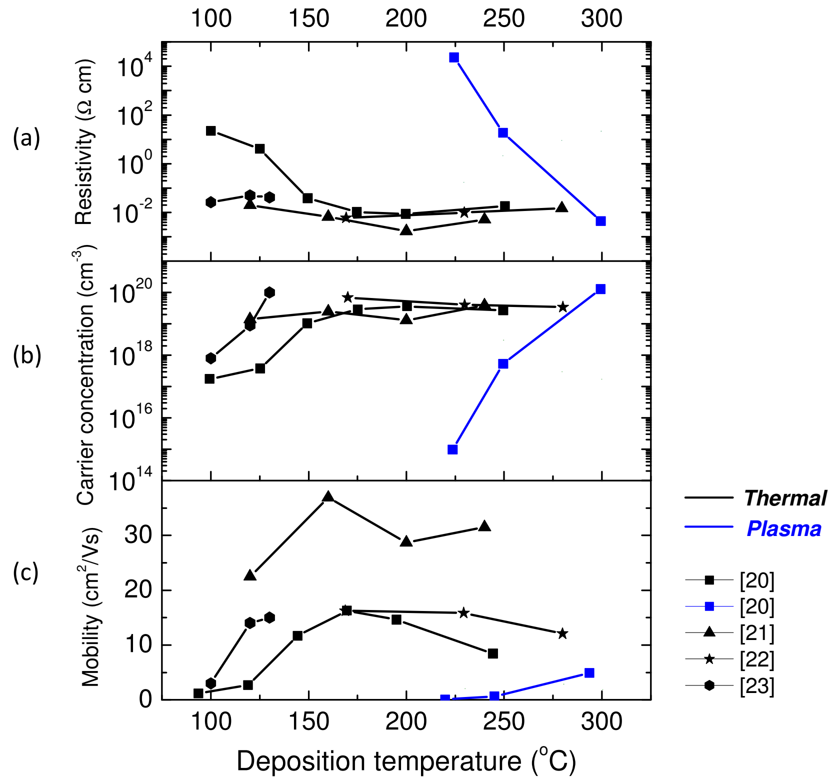

Figure 3.9 *Electrical properties as a function of deposition temperature from the literature. These values were measures at different thicknesses, reactors and conditions (a) Resistivity (b) Carrier concentration (c) Mobility*

The resistivity in Figure 3.8a was immeasurably high for both processes at deposition temperatures of 50 and 100 °C. This is indicated with dashed lines. For the thermal process the resistivity decreased rapidly at temperatures above 100 °C. A minimum value of $5 \cdot 10^{-2}$ Ω cm was observed at 200 °C. At temperatures above 250 °C the resistivity increased again.

The plasma-assisted process showed resistivity values between $3 \cdot 10^{+1}$ and $1 \cdot 10^{+2}$ Ω cm, in the temperature interval of 100 - 350 °C. At temperatures above 350 °C the resistivity increased.

The thermal process literature values in Figure 3.9a show the same trend as the measured curve. That is, a high resistivity starting at temperatures around 100 °C and decreasing to a minimum value of approximately 10^{-2} Ω cm around 200 °C. Above 200 °C the resistivity increased again. The literature curves of Figure 3.9b,c show that the decreasing resistivity was caused by both an increasing carrier concentration and mobility. The carrier concentration showed an increase of two orders of magnitude and the mobility showed an increase of one order of magnitude. This means that the increasing carrier concentration was the dominant effect in resistivity variation with temperature.

The plasma-assisted literature curve exhibits immeasurably high resistivity values at temperatures below 225 °C. At temperatures above 225 °C the resistivity steeply decreased due to a increase in carrier concentration. A minimum resistivity value in the order of 10^{-3} Ω cm was observed at a temperature of 300 °C. This literature curve is inconsistent with the measured curve. It is conspicuous that there is only one report on the electrical properties plasma-assisted processes. Perhaps resistivity values were often immeasurably high end therefore not published.

The thermal process exhibits a significantly lower resistivity than the plasma-assisted process. The difference was 3 to 4 orders of magnitude in the temperature range of 150 - 300 °C. Therefore, the thermal process seems to be preferable for the applications mentioned in Chapter 1. The thermal process resistivity even showed some sort of temperature window between deposition temperatures of 150 and 250 °C. Resistivity fluctuations within this window were between $1{\cdot}10^{-2}$ and $3{\cdot}10^{-2}$ Ω cm. These minimum resistivity values were above the desired 10^{-3} Ω cm as Chapter 1 described. This is the reason to apply doping, as described in Chapter 4.

3.2.6 Transmittance

Figure 3.10 shows the measured transmittance of the deposited ZnO films for different deposition temperatures.

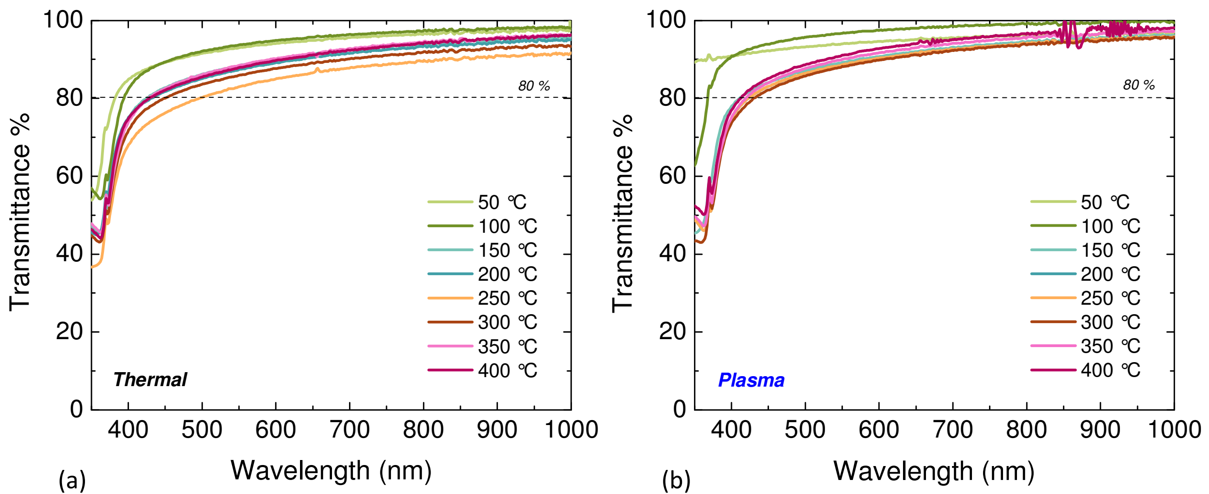

Figure 3.10 *Transmittance as a function of wavelength for different deposition temperatures. All samples had a thickness of approximately 40 nm. (a) shows the transmittance for the thermal process and (b)for the plasma-assisted process.*

Figure 3.10a shows that the thermal process transmittance is highest at deposition temperatures of 50 and 100 °C. This relates to the high resistivity values caused by low carrier concentration as shown in section 3.2.5. Free carriers are known to reduce transmittance. The overall transmittance was above 80 % for wavelengths above 455 nm. An exception is the 250 °C curve. This curve exceeds 80 % only above 500 nm. All transmittance values were above 0 %, even at wavelengths below the optical band gap. The reason was that the 40 nm films are too thin to absorb all light.

The transmission graph of the plasma-assisted process in Figure 3.10b also shows the highest values for deposition temperatures of 50 and 100 °C. An interesting phenomenon was that the 50 °C curve showed no transmittance drop at wavelengths below the optical band gap of approximately 365 nm. This raises the question whether 40 nm was really deposited on the glass sample at this temperature. Maybe the low temperature caused the thermal energy component of the reaction to be insufficient for decent growth. In that case less than 40 nm would be deposited, which would explain the high transmittance. All other temperatures lie close to each other and showed to be above 80 % for wavelengths above 435 nm. This 435 nm is lower than the thermal process limit of 455 nm.

In terms of transmittance the thermal and plasma-assisted processes showed to be similar.

3.2.7 Optical Band Gap

Figure 3.11 shows $(\varepsilon_2 \cdot E^2)^2$ as a function of photon energy E, for different deposition temperatures. The optical band gap (Tauc gap) is defined as the photon energy, where the extrapolation of the linear part of this parameter, intersects the line $(\varepsilon_2 \cdot E^2)^2 = 0$ [42]. Note that the dielectric functions were modelled by a B-spline.

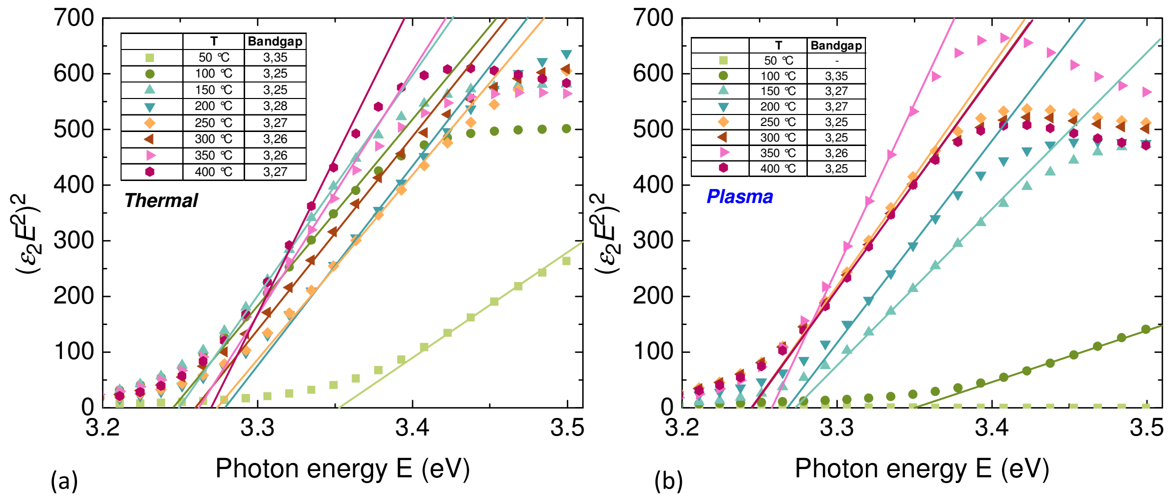

Figure 3.11 *$(\varepsilon_2{\cdot}E^2)^2$ as a function of photon energy for different deposition temperatures. The optical band gap is defined as the photon energy, where the extrapolation of the linear part of this parameter, intersects the line $(\varepsilon_2{\cdot}E^2)^2 = 0$ All samples had a thickness of approximately 40 nm (a) Thermal process (b) Plasma-assisted process.*

Both graphs show a relatively high band gap of approximately 3.5 eV up to deposition temperatures of 100 °C. For the plasma assisted process there was no observable band gap at 50 °C, which matches the transmittance date in Figure 3.10b. For higher temperatures the band gap showed no clear temperature dependence and band gap values were approximately 3.25 eV. The measurement technique was based on ε_2 values which is an absorbance related quantity. Perhaps the low thickness of 40 nm, together with the low carrier concentrations, caused this measurement method to be inaccurate for lower deposition temperatures since there was not enough absorbance to measure the band gap appropriately. This might be the cause of the higher band gap values that were measured at lower deposition temperatures.

3.2.8 Crystalinity

Figure 3.12 shows the XRD data for deposition temperatures.

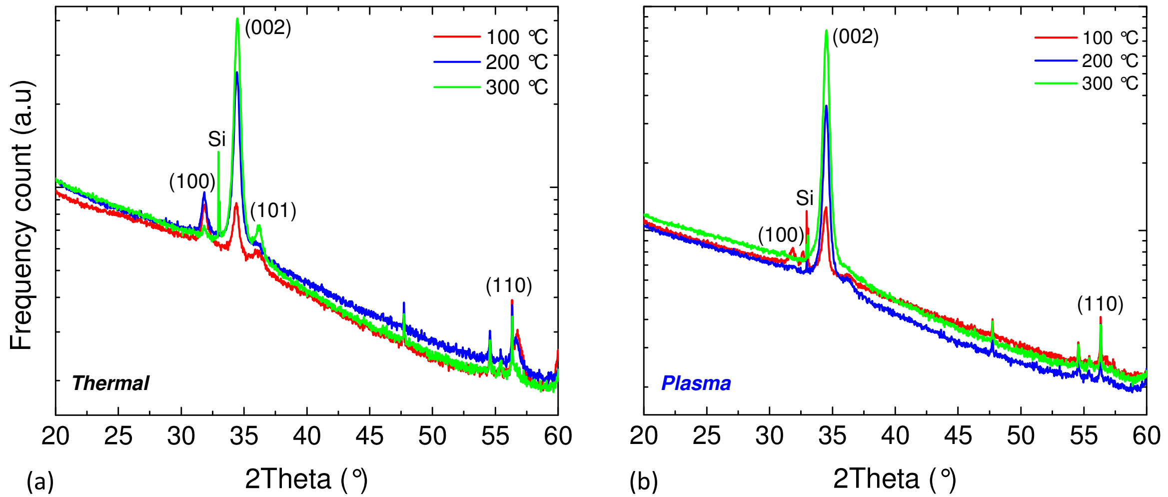

Figure 3.12 *XRD data for different deposition temperatures. The layer thickness was approximately 75 nm (a) Thermal process (b) Plasma-assisted process*

The thermal process in Figure 3.12a shows no preferred orientation at a deposition temperature of 100 °C, because peaks were observed at *(100)*, *(002)* and *(110)*. At higher deposition temperatures the *(002)* peak becomes dominant, indicating that there was a transition to a preferred orientation which was enhanced by deposition temperature. The prominent *(002)* peaks indicated that the crystallite structure of the films were mainly oriented with their c-axis perpendicular to the substrate plane.

The plasma-assisted process in Figure 3.12b shows a preferred *(002)* orientation at every deposition temperature. The size of the peak grew with increasing deposition temperature indicating that the *(002)* direction was enhanced with increasing deposition temperature.

3.3 Conclusions and Outlook

Thermal and plasma-assisted ALD processes were developed for intrinsic ZnO. The thermal process was shown to be good in terms of growth and non-uniformity. The thermal process was therefore considered to form a solid base for future research and applications like the ones that were mentioned in Chapter 1. The thermal process resistivity values however, can be further optimized by doping. Chapter 4 will elaborate on the Al doping of the thermal process.

The plasma-assisted process showed a lower GPC, a very high non-uniformity and a high resistivity compared to the thermal process. Also a large soft saturation component was observed, which means that a very long plasma dosing time was necessary in order to reach saturation. These challenges must be overcome before the full potential of the plasma-assisted ALD process can be utilized. A suggestion would be to study the growth characteristics of the process more closely, i.e studying the saturation behaviour. Two experiments can be proposed for this. First the O content of a series with different plasma dosing could be measured. This would tell whether a longer plasma dose incorporates extra O, which can cause additional growth. Secondly, depositions could be done with the plasma power turned off. This would tell whether O_2 acts as a reactant that causes an additional thermal growth component.

Chapter 4

Aluminium Doping of Zinc Oxide

4.1 Introduction

Chapter 3 showed that thermal ALD layers of intrinsic zinc oxide exhibited very growth characteristics and film properties. Only a small nucleation delay was observed and layers showed only moderate non-uniformity. Minimum resistivity values in the order of 10^{-2} Ω cm were found, while obtaining a transmittance above 80 % in the visible spectrum. These results were found for layers of 40 nm thickness, which is a typical value for ALD applications. The applications that are mentioned in Chapter 1 however, require resistivity values below 10^{-3} Ω cm. Therefore, aluminium doping was applied to reduce the resistivity. With aluminium doping a number of Zn atoms are replaced by Al. Al atoms contribute a valence electron as a charge carrier. The resulting extra charge carriers reduce the electrical resistivity. Care must be taken to preserve the material transmittance. Free carriers can interact with incoming electromagnetic waves, causing the transmittance to decrease mainly in the infrared region. This interaction can be described by the Drude model [43].

4.1.1 Literature Overview of Aluminium Doped ZnO by ALD

A number of publications report on the ALD of aluminium-doped ZnO (AZO or ZnO:Al) [28-41]. Different reactors and conditions such as substrate material, substrate temperature and layer thickness were used to produce AZO samples. In all cases the samples were deposited with thermal ALD using trimethyl-aluminium as the Al precursor. The properties of the samples were determined as function of Al fraction. Different methods were described for measuring the Al fraction. A first example is measuring by *inductively-coupled plasma atomic emission spectroscopy* (ICP AES) [32], on a dissolved material sample. A second example is estimating the Al fraction based on the Zn/Al cycle ratio. Figures 4.1 and 4.2 show a selection of literature values for electrical properties and transmittance. Table 4.1 shows the relevant settings that were used.

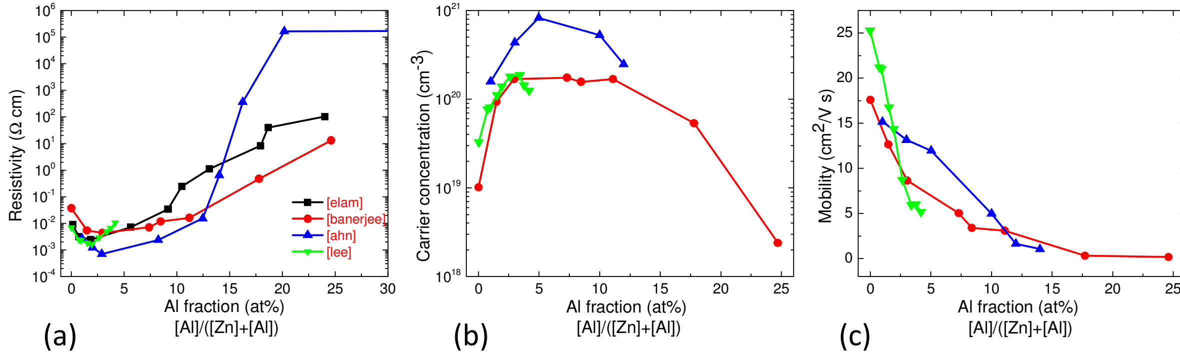

Figure 4.1 *Selection of reported electrical properties of AZO layers. (a) Resistivity (b) Carrier concentration (c) Mobility. Table 4.1 shows the relevant settings that were used while obtaining these results .The Al fraction indicated the number of Zn atoms that are replaced by Al atoms and is therefore defined as [Al]/([Zn]+[Al])*

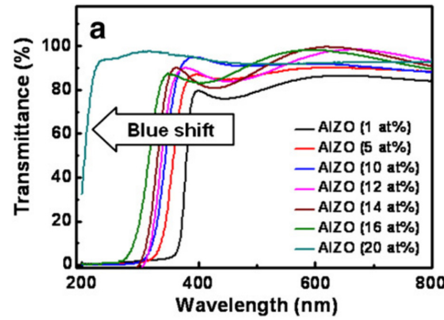

Figure 4.2 *Measured transmittance as function of aluminium percentage. Data from Ahn et al. [28].*

Table 4.1 *Relevant settings of selected literature*

Reference	Sample thickness (nm)	Deposition temperature (°C)	Method of Al % determination
Elam et al. [32]	74-80	177	ICP-plasma atomic emission spectroscopy
Banerjee et al. [29]	100	150	Estimation based on Zn/Al cycle ratio
Ahn et al. [28]	200	200	Estimation based on Zn/Al cycle ratio
Lee et al. [30]	41-45	200	Estimation based on Zn/Al cycle ratio

The selected literature studies showed similar results. Figure 4.1a shows that the resistivity initially decreased with increasing aluminium fraction. A minimum resistivity was obtained around 3 at % aluminium. The resistivity increased again with higher aluminium fraction. The mechanism that caused this behaviour will be explained in section 4.5. The minimum resistivity value was approximately 10^{-3} Ω cm. This is close to the required value for the applications that were mentioned in Chapter 1.

The transmittance results of the different literature studies were also similar to each other. Transmittance values were most often above 80 % in the 400-800 nm wavelength region. This is shown by the example in Figure 4.2. The band gap showed a blue shift with increasing aluminium fraction. The mechanism behind this phenomenon will be explained later in this chapter.

In all literature on the ALD of AZO, *trimethyl-aluminium* (TMA) was used as aluminium precursor.

4.1.2 Aluminium Precursors

Trymethyl-aluminium (TMA), $[Al(CH_3)_3]$, is a popular aluminium precursor as it exhibits almost ideal ALD characteristics [15,51]. However, its main drawback is its highly pyrophoric nature [51]. The search for safer precursors for use in industrial-scale, high-volume manufacturing is ongoing.

A promising alternative is *Dimethyl-aluminium isoproxide* $[Al(CH_3)_2(\mu\text{-}O^iPr)]_2$ (DMAI) where ^iPr = isopropyl. This precursor is reported to be stable, non-pyrophoric and therefore potentially safer than TMA [51]. Table 4.2 shows several properties of TMA and DMAI. DMAI was shown to be a comparable aluminium precursor to TMA for deposition of Al_2O_3, down to deposition temperatures of 150 ^oC [51].

In this thesis both TMA and DMAI were used for the ALD of aluminium-doped ZnO. The precursors were compared by evaluating the resulting properties of the samples.

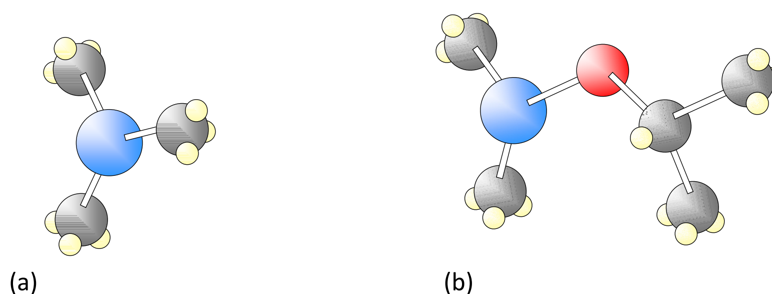

Figure 4.3 *Aluminium precursors depicted as monomers. In reality they are dimeric [51] (a) TMA (b) DMAI. Blue = Al, black = C, white = H, red = O*

Table 4.2 *Properties of TMA and DMAI* [51]

Precursor property	TMA	DMAI
Physical state (R.T.)	Liquid	Liquid
Melting point	15 °C	< R.T.
Boiling point	125 °C	172 °C
Decomposition temperature	~330 °C	~370 °C
Vapour pressure	9 Torr at 17 °C	9 Torr at 67 °C
Pyrophoric	Yes	No

4.1.3 Measuring Al Fraction with Spectroscopic Ellipsometry

Spectroscopic ellipsometry (SE) can potentially be used to measure the doping concentration. Longo et al. studied the deposition of Strontium titanate, $SrTiO_3$ (STO) [52]. Films with different Sr/Ti ratios were produced by combining *x* ALD cycles of SrO with *y* cycles of TiO_2. The Sr/Ti ratio was measured by *Rutherford backscattering spectroscopy* (RBS). The dielectric functions ε_1 and ε_2 of SrO and TiO_2 films, as well as those of STO films deposited with different SrO/TiO_2 cycle ratios, were measured by SE. Figure 4.4 shows that the dielectric functions of STO were homogeneously distributed between those of SrO and TiO_2. The measured dielectric functions and RBS data were combined in a CompleteEASE *material library*. The dielectric function of any STO layer can be compared to the material library in order to determine the Sr/Ti ratio.

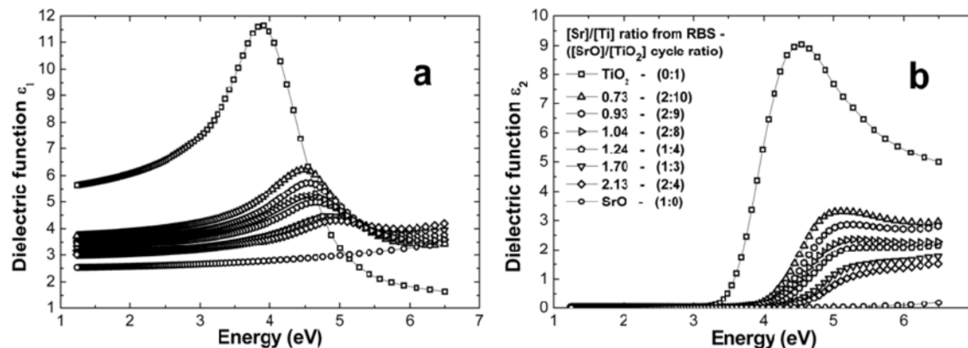

Figure 4.4 *Dielectric functions (a) ε_1 and (b) ε_2 of SrO, TiO_2 and STO films. The corresponding Sr/Ti ratios from RBS and SrO/TiO_2 cycle ratios are indicated as well. The dielectric functions of STO were homogeneously distributed between those of SrO and TiO_2 [52].*

Figure 4.5 shows the dielectric functions ε_1 and ε_2 of ZnO and Al_2O_3 layers. Both dielectric functions were measured for 40 nm thick, thermal ALD layers that were deposited using OpAL^{TM} at 150 ^{o}C. The dielectric functions were fitted with a B-spline model. Figure 4.5 shows that the dielectric functions of ZnO are clearly distinguishable from those of Al_2O_3. Section 4.5.2 will show that during doping, a part of the incorporated Al atoms does not replace Zn atoms, but will form Al_2O_3 instead. This means that during doping, the material becomes a composition of both ZnO and Al_2O_3. This situation is analogous to the STO film composition that Longo et al. studied. AZO layers were therefore expected to show intermediate dielectric functions between those of ZnO and Al_2O_3. An AZO material library could then be built, which can be used to determine the aluminium fraction directly from the SE data. SE measurements are relatively straightforward take and could potentially save a lot of (expensive) analysis, such as *Rutherford Backscattering Spectroscopy* (RBS).

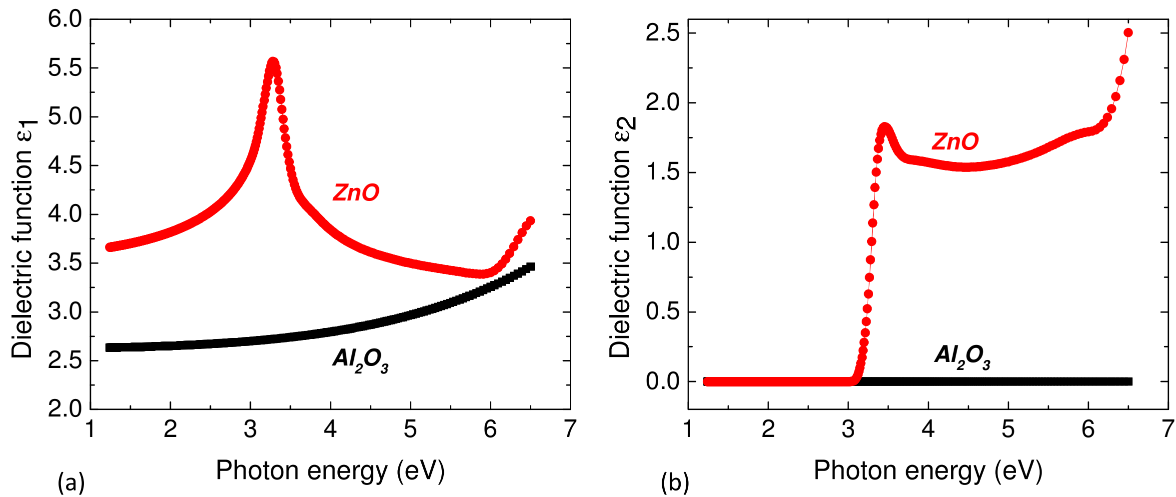

Figure 4.5 *Dielectric functions of ZnO and Al_2O_3. (a) ε_1 (b) ε_2.The dielectric functions of both materials are clearly distinguishable in their form. AZO layers, which are a composed of both ZnO and Al_2O_3, may show intermediate forms of these dielectric functions. In that case a material library can be built within CompleteEase, which can be used to determine the Al concentration with SE*

4.1.4 Goals

The goal was to develop ALD processes of aluminium doped ZnO, using both TMA and DMAI as aluminium precursors. The growth, Al incorporation, electrical properties and optical properties of these processes were then compared. The differences between the two processes were explained with the differences in chemical composition of the precursors. Finally, AZO material libraries were built in CompleteEASE. With the help of these material libraries the Al fraction of arbitrary samples can be determined with SE. This chapter will only report the results of the thermal ALD process.

4.2 Experimental

AZO layers were deposited by inserting one Al_2O_3 cycle after every *n* ZnO cycles. This constituted one *super-cycle*. A number of super-cycles were repeated to achieve the desired thickness. The mechanism is depicted in Figure 4.6.

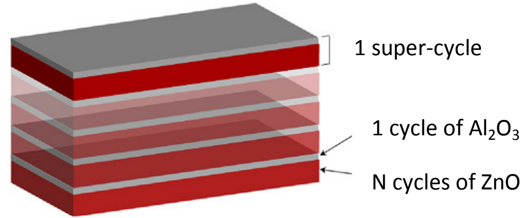

Figure 4.6 *Representation of doping method. One cycle of Al_2O_3 was deposited after n ZnO cycles to constitute a super-cycle. A number of super-cycles was repeated to achieve the required layer thickness. Picture used from [30].*

The aluminium fraction was estimated by the following ratio of ZnO and Al_2O_3 *growth per cycle* (GPC) values, which is the same method as described in the literature [28-30,32]:

$$\text{(Nominal) } Al\ fraction = \frac{[Al]}{[Al]+[Zn]} = \frac{GPC_{Al2O3}}{GPC_{Al2O3} + n \cdot GPC_{ZnO}} \cdot 100\% \qquad (4.1)$$

Where, for a deposition temperature of 150 ^{o}C, GPC_{TMA} = 0.10 nm/cycle and GPC_{DMAI} = 0.07 nm/cycle [51]. GPC_{DEZ} = 0.21 nm/cycle as was reported in Chapter 3. The aluminium fraction that was determined by formula (4.1) is called *nominal aluminium fraction*. This indicates that the value is an estimate. The number of super-cycles was determined by:

$$N_s = \frac{d}{GPC_{Al2O3} + n \cdot GPC_{ZnO}} \qquad (4.2)$$

Where *d* is the required layer thickness.

Samples of 40 nm thickness were deposited at 150 °C, on silicon and glass substrates. The nominal aluminium fraction was varied between 0 and 6 %.

Table 4.3 shows the Al_2O_3/ZnO cycle ratios, number of super-cycles and resulting thicknesses of the deposited series. Appendix B contains the ALD recipes of both the TMA and DMAI Al_2O_3 processes.

The thickness and transmittance were measured by SE, whereas *four-point probe* (4pp) and Hall measurements were carried out to determine the electrical properties. SE and Hall measurements were taken within one hour after deposition to exclude aging effects. RBS was used on a selection of samples to determine the aluminium fraction. XPS was also used to determine the aluminium fraction.

Table 4.3 *Deposition cycles for thermal processes*

Nominal Al %	TMA			DMAI		
	ZnO cycles per super-cycle	Super-cycles	Obtained thickness (nm)	ZnO cycles per super-cycle	Super-cycles	Obtained thickness (nm)
0	-	-	40.1	-	-	40.9
1	35	6	42.8	37	5	36.5
2	17	12	39.6	18	14	48.4
3	11	20	41.9	12	20	44.0
4	8	29	41.5	9	27	44.6
5	7	33	40.3	7	34	41.5
6	5	60	39.6	6	39	38.6

4.3 ZnO Growth Delay After Al_2O_3 Cycle

Formula (4.2) was used to calculate the number of super-cycles needed for a sample thickness of 40 nm. The thickness that was measured by SE deviated from the prediction. This deviation was proportional to the number of super-cycles and therefore, to the nominal aluminium fraction. This is shown for the thermal TMA doping process in Figure 3.7a. The phenomenon however, was observed the thermal DMAI process as well. Figure 3.7b shows that there was no thickness deviation in the TMA plasma-assisted process. Note however, that this figure constitutes the only analysis of the plasma-assisted doping process in this chapter. The plasma-assisted doping process will not be further elaborated. Also note that the super-cycle values in Table 4.3 were corrected for the growth delay effect. This means that the super-cycles values that were shown produced correct thickness results of approximately 40 nm.

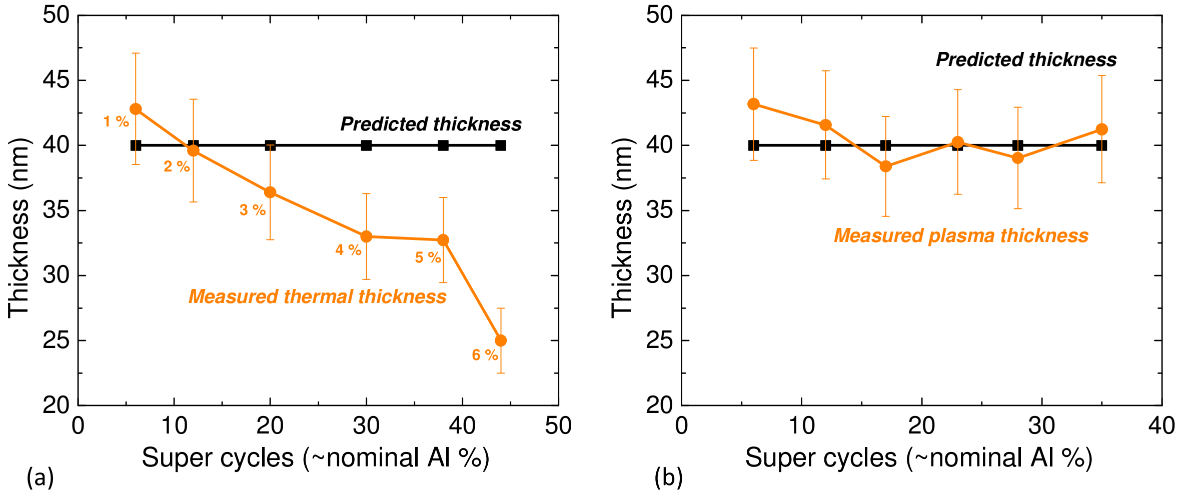

Figure 4.7 *Measured and predicted thickness as a function of the number of super-cycles, for the TMA doping process (a) Thermal (b) Plasma-assisted. Only the thermal process showed a deviation in thickness that was proportional to the number of super-cycles and therefore to the nominal aluminum fraction.*

The observed thickness deviation indicated that the predicted GPC of combined cycles, that was based on reported bulk GPCs, was not accurate, i.e.,

$$GPC_{(n \cdot ZnO + Al_2O_3)} \neq n \cdot GPC_{ZnO} + GPC_{Al_2O_3} \tag{4.3}$$

This means that the ZnO and Al_2O_3 layers influenced each other. To study the combined growth more closely, SE measurements were taken after each cycle, for the duration of 5 super-cycles. In this case a super-cycle comprised 11 ZnO cycles and 1 Al_2O_3 cycle. A 15 super-cycle base layer of approximately 30 nm was deposited prior to the measurements. A total layer thickness above 30 nm, guaranteed that optical constants and thickness parameters were uncorrelated within the SE Cauchy model. This condition was necessary to obtain accurate thickness results from a backwards fit. In a backwards fit, the average optical constants of the ZnO and Al_2O_3 layers were used for thickness fitting.

Figures 4.8 and 4.9 show the results of the TMA and DMAI processes respectively. Figures 4.8a and 4.9a show the film thickness after each cycle. ZnO cycles are presented in orange and Al_2O_3 in black. The thickness values of each subsequent cycle were subtracted from each other to obtain the GPC, which is shown in Figures 4.8b and 4.9b. Note that the GPC curves showed some noise which was mostly visible in the TMA process.

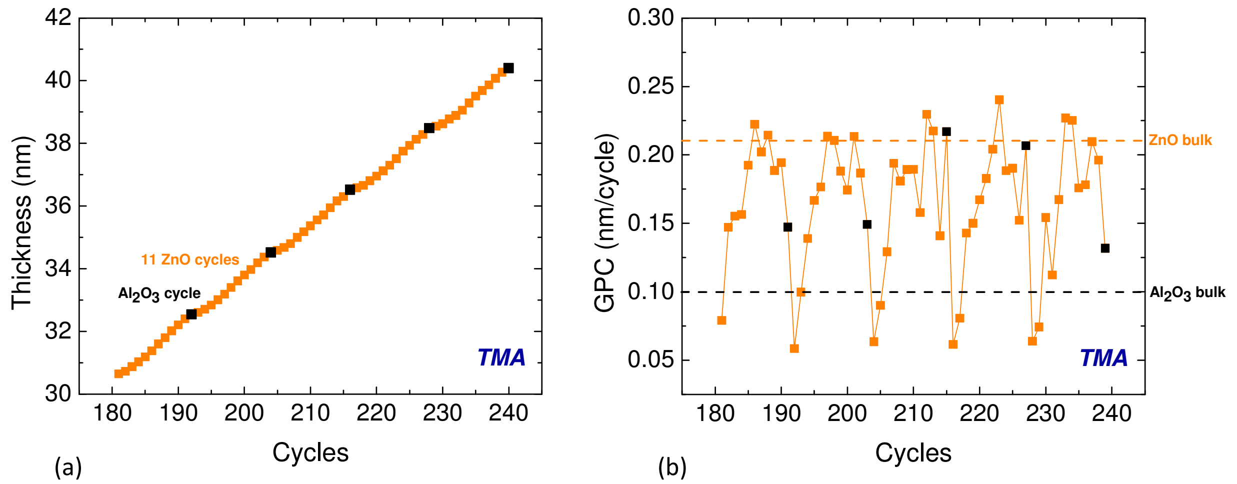

Figure 4.8 *Combined growth of ZnO and Al_2O_3 cycles, with TMA as aluminium precursor. The thickness was measured after each cycle, for the duration of 5 super-cycles. A 15 super-cycle base layer was deposited prior to the experiment. The ZnO/Al_2O_3 cycle ratio was 11/1. (a) Thickness (b) growth per cycle. The ZnO GPC was inhibited after each Al_2O_3 cycle*

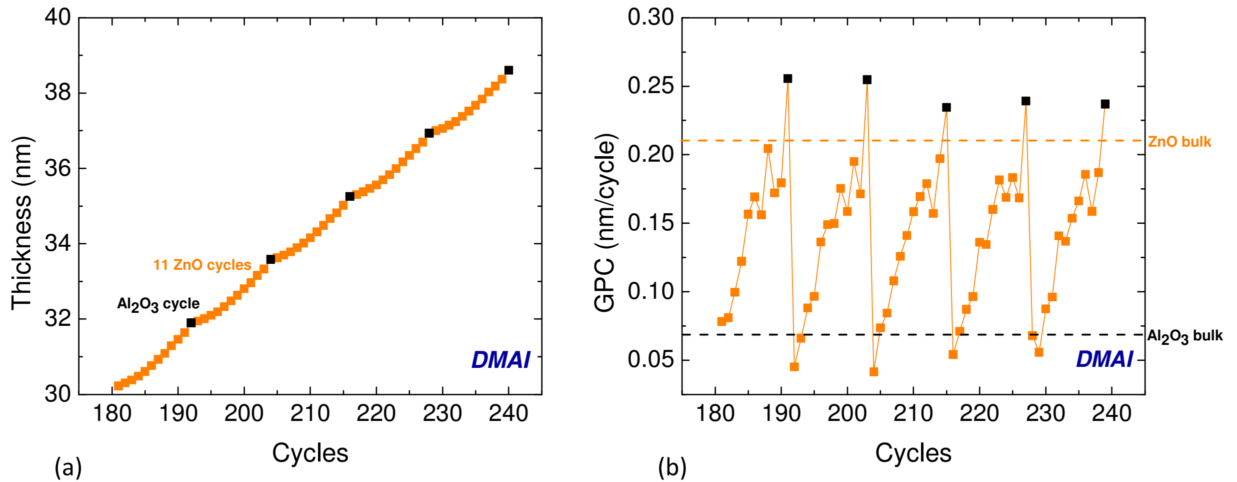

Figure 4.9 *Combined growth of ZnO and Al_2O_3 cycles, with DMAI as aluminium precursor. The thickness was measured after each cycle, for the duration of 5 super-cycles. A 15 super-cycle base layer was deposited prior to the experiment. The ZnO/Al_2O_3 cycle ratio was 11/1. (a) Thickness (b) growth per cycle. The ZnO GPC inhibited after each Al_2O_3 cycle*

Figures 4.8a and 4.9a show that the ZnO growth is inhibited after each Al_2O_3 cycle. Reduced ZnO GPCs after TMA cycles were already reported in literature and were primarily believed to result from a decreased number of reaction sites [31,36]. A possible mechanism that results in a decreased number of reaction sites is related to the relative acidity of the ZnO and Al_2O_3 surfaces [31]. The ZnO surface is basic and the Al_2O_3 surface is nearly neutral. During the transition between ZnO and Al_2O_3, the ZnO and Al_2O_3 hydroxyls will coexist in the alloy film surface. The coexistence may allow a proton exchange surface reaction to occur, which is also shown in Figure 4.10 and is commonly referred to as a Brønsted-Lowry acid-base reaction.

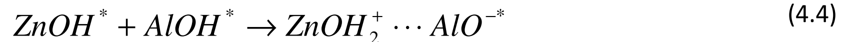

$$ZnOH^{*} + AlOH^{*} \rightarrow ZnOH_2^{+} \cdots AlO^{-*} \tag{4.4}$$

* denotes species at the surface. The hydrogen bond complex $ZnOH_2^{+} \cdots AlO^{-*}$ might deactivate the surface hydroxyl groups and render them less reactive to the ZnO cycle.

The relatively high activation energy of the plasma may affect the number of OH groups and/or cause the plasma-assisted process to be less sensitive to the number of OH groups. This may result in the plasma-assisted ZnO growth to be normal.

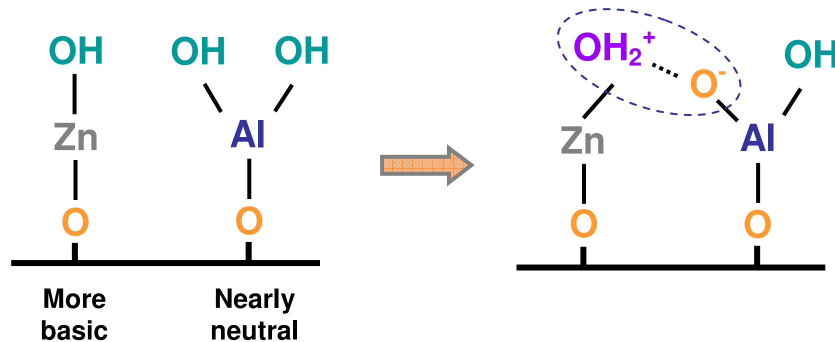

Figure 4.10 *Proposed mechanism to explain the inhibited growth of ZnO after an Al_2O_3 cycle [31]. The ZnO surface is relatively basic compared to the Al_2O_3 surface. During transition between ZnO and Al_2O_3, the ZnO and Al_2O_3 hydroxyls coexist in the film surface. The coexistence may allow a proton exchange reaction to occur in which a hydrogen bond is formed. This hydrogen bond might deactivate the surface hydroxyl groups and render them less active to the ZnO cycle.*

Etching of the ZnO by the aluminium precursor was mentioned as a second possible cause of the inhibited ZnO growth [31].

The hydrogen bond forming and etching that were described by Elam et al. may contribute to the inhibited ZnO growth after each Al_2O_3 cycle. Figures 4.8b and 4.9b however, show some additional effects that were different for both aluminium precursors:

1. After an Al_2O_3 cycle, the ZnO GPC dropped to an average value of 0.07 nm/cycle with a 0.01 nm/cycle standard deviation and 0.05 nm/cycle with a 0.01 nm/cycle standard deviation for the TMA and DMAI process respectively;
2. After each Al_2O_3 cycle, the ZnO required a number of cycles to restore to its bulk GPC of 0.21 nm/cycle. After TMA this was approximately 6 cycles and after DMAI this was above 11 cycles;
3. The Al_2O_3 GPCs were higher than the reported bulk values. The average TMA GPC was 0.17 nm/cycle with a 0.04 nm/cycle standard deviation, while the reported bulk value was 0.10 nm/cycle. The average DMAI GPC was 0.24 nm/cycle with a 0.01 nm/cycle standard deviation, while the reported bulk value was 0.07 nm/cycle.

These findings indicated that the ZnO growth was more strongly inhibited after a DMAI cycle. Also the difference between bulk and single cycle Al_2O_3 GPC was largest for DMAI. These differences between the TMA and DMAI process may be a result of the difference in precursors. The following hypothesis provides a possible explanation of the mechanism that could cause these differences:

Figure 4.11 depicts the ideal ALD process of Al_2O_3 on ZnO, for both TMA and DMAI.

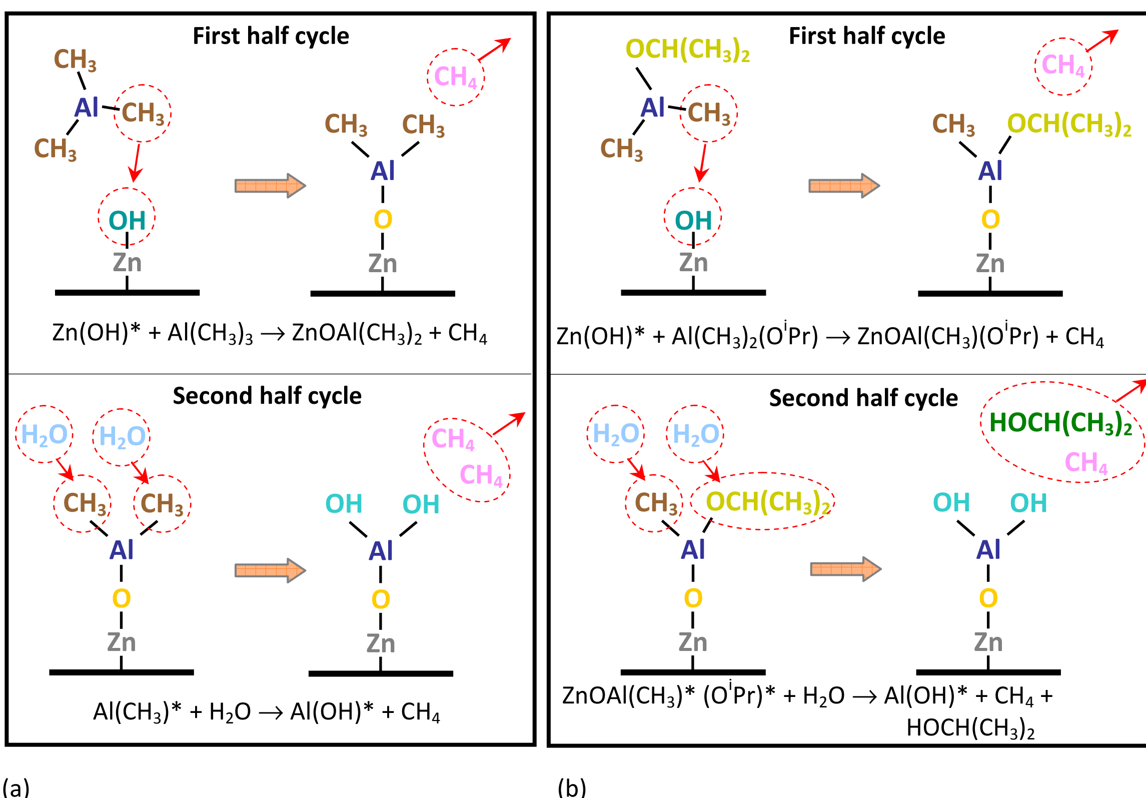

(a) (b)

Figure 4.11 *Ideal monofunctional ALD process cycles of Al_2O_3 on ZnO. (a) TMA (b) DMAI*

In the ideal processes of Figure 4.11, all OH groups react with precursor molecules during the first half cycle. During the second half cycle, all ligands react with water molecules. In reality however, deviations from ideal behaviour are likely to occur. The Al-O dissociation energy of 501.9 kJ/mol is relatively large compared to the Al-C dissociation energy of 267.7 kJ/mol [53]. This means that $OCH(CH_3)_2$ ligands are more tightly bonded to Al than CH_3 ligands. $OCH(CH_3)_2$ ligands therefore could possibly be more likely to remain present in the material, at least for some number of subsequent water doses. The presence of these ligands could have caused the additional effects that were shown in Figures 4.8b and 4.9b.

When ligands remain in the material after the DMAI cycle, they substitute OH groups that would have been formed in the case where these ligands were completely removed. The resulting decrease in OH group density would lead to a relatively strong inhibited ZnO growth after a DMAI cycle. Remaining $OCH(CH_3)_2$ ligands are also relatively large compared to CH_4 ligands. Therefore they would be likely to cause steric hindrance during subsequent ZnO cycles. Steric hindrance, which was also described by Puruunen et al. [18], can inhibit the ZnO growth as well. A decreased OH group density and steric hindrance, both caused by a relatively large number of large remaining

$OCH(CH_3)_2$ ligands, could possibly explain the difference in ZnO growth after DMAI and TMA cycles (points 1 and 2 of the phenomena in Figures 4.8a and 4.9a).

The remaining ligands and/or OH groups after the second half cycle would also add to the material thickness and could therefore be detected by SE. This could cause the single cycle GPC value, which was measured by SE, to be higher than the bulk GPC value that was found earlier. This effect may have caused the Al_2O_3 GPC values to appear higher than the bulk GPCs, which was point 3 of the phenomena in Figures 4.8a and 4.9a. Since $OCH(CH_3)_2$ ligands are larger than OH groups, this additional GPC would be highest for DMAI.

For the doping experiments the DMAI recipe was used that was developed by Potts et al. [51]. Note that for this recipe, no H_2O saturation curve was measured. The same H_2O dose was chosen as for the TMA process. However, $OCH(CH_3)_2$ ligands in DMAI are more strongly bonded than TMA ligands in TMA. This means that the chosen H_2O dose might not have been long enough to ensure saturation. This could indicate that the hypothesis of remaining DMAI ligands is true.

The hypothesis of remaining $OCH(CH_3)_2$ ligands can be tested with in-situ *quartz crystal microbalance* (QCM). QCM can be used to determine the mass of deposited material after each cycle. With this technique any remaining ligands can be detected. Determining the presence of material impurities can be interesting as well. Carbon impurities, for instance, could be present when ligands remain in the material. A carbon depth profile can be measured with XPS for this purpose. RBS can also provide information about the carbon content. RBS measurements however, showed no evidence of carbon in the films. However, the carbon detection limit was approximately 5 at %, which was relatively high and could be the reason that a low carbon content was not observed.

4.4 Aluminium Fraction

The nominal aluminium fraction was compared to values measured by RBS and XPS. Figure 4.12 shows the results for both TMA and DMAI processes. XPS spectra are sensitive to the chemical environment of the measured species, which makes fitting, and therefore precise quantification, relatively complicated. RBS spectra are not sensitive to the specific chemical environment of the species. RBS is therefore commonly accepted to be more accurate than XPS for quantitative elemental analysis of thin films. Figure 4.12 shows however, that RBS and XPS data match reasonably well, at least for nominal Al fractions up to 4 %. XPS data will be used for the remaining analysis in this thesis.

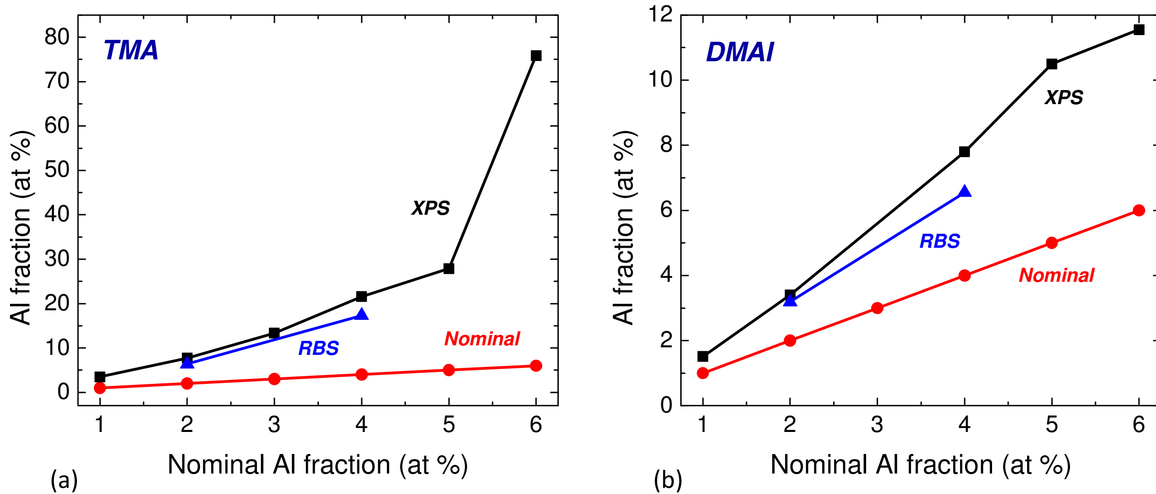

Figure 4.12 *Al fraction measured by RBS and XPS, as a function of nominal Al fraction. (a) TMA process (b) DMAI process. Note the difference in vertical scales.*

Figure 4.12 shows that the measured Al fraction, in general, was higher than the nominal Al fraction. The difference between measured and nominal Al fraction, increased with increasing nominal Al fraction. These differences were largest for the TMA process.

The difference between measured and nominal Al fraction can be explained by the average Al_2O_3 and ZnO GPCs. The nominal Al fraction was calculated by formula (4.1). Bulk GPC values were used in this calculation. Figures 4.8a and 4.9a showed that the ZnO growth was inhibited after each Al_2O_3 cycle. This caused the average ZnO GPC to be less than the bulk value. The difference between average and bulk ZnO GPCs increased with nominal Al fraction, since more Al_2O_3 cycles were inserted. It was this deviation between bulk GPCs and actual average GPCs that caused a higher amount of aluminium to be incorporated.

The difference between measured and nominal Al fractions, between TMA and DMAI processes, was probably caused by steric hindrance during the first Al_2O_3 half cycle. Figure 4.13 shows that the relatively large $OCH(CH_3)_2$ ligands are more likely to obstruct OH groups, compared to the CH_4 ligands. This caused more aluminium atoms to be deposited in a TMA cycle, than in a DMAI cycle. This is probably the same effect that causes the different bulk GPCs of both processes.

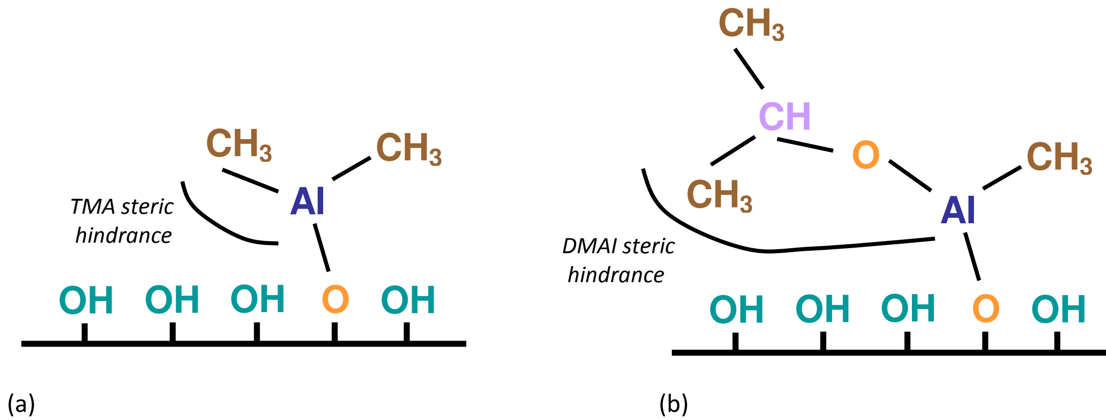

Figure 4.13 *A schematic representation of steric hindrance during the first Al_2O_3 half cycle. (a) TMA process (b) DMAI process. The DMAI ligands exhibits the largest steric hindrance because of the largest ligands. This causes fewer Al atoms to be deposited each cycle.*

4.5 Electrical Properties

4.5.1 Measurement Results

Figure 4.12 shows the electrical properties of the films deposited using both the TMA and DMAI processes. Resistivity values were determined by 4pp and Hall measurements. Mobility and free carrier concentration were also obtained by Hall measurements. Figure 4.12a shows some deviation between 4pp and Hall resistivity values. The 4pp values were generally higher than the Hall values. The 4pp resistivity values were taken within one hour after deposition and were therefore considered to most accurately represent the as-deposited properties. Hall measurements were taken weeks after deposition and may include aging effects. Nevertheless, the trends in mobility and free carrier concentration could be used to explain the behaviour of resistivity versus Al fraction.

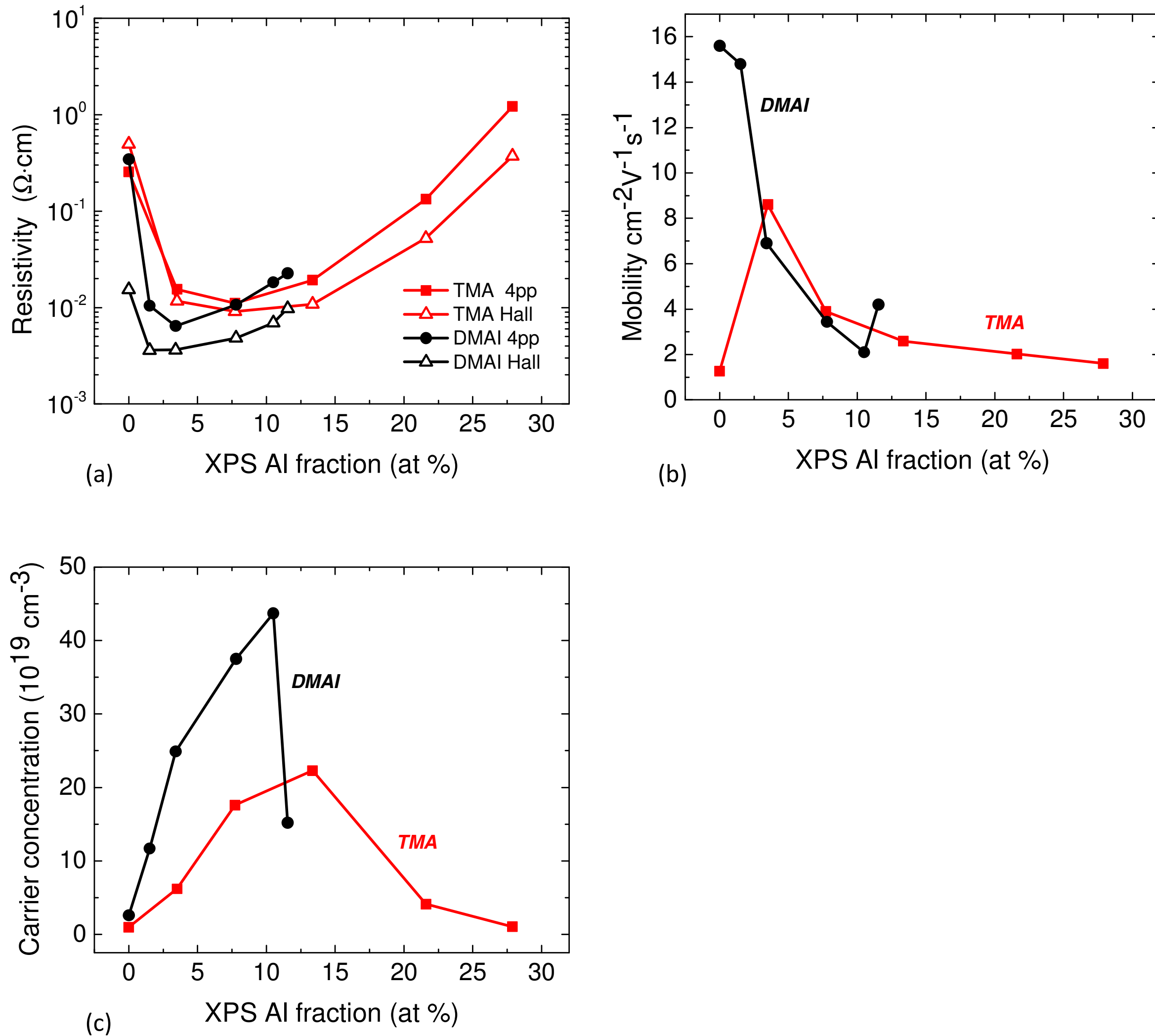

Figure 4.14 *Electrical properties measured for both TMA and DMAI processes. (a) Resistivity (b) Mobility (c) Free carrier concentration*

Figure 4.12a shows that the resistivity initially decreased with Al fraction. Minimum 4pp values of $1.2 \cdot 10^{-2}$ and $6.5 \cdot 10^{-3}$ Ω cm were measured for TMA and DMAI respectively. The minimum values were found at approximately 3 % Al fraction. The resistivity gradually increased again with further Al fraction. Between Al fractions of 10 and 15 %, the resistivity started to increase rapidly. Note that the resistivity at 0 % Al fraction was found to be approximately 0.3 Ω cm, while the intrinsic thermal resistivity in Chapter 3 was found to be 0.03 Ω cm. This difference may have been caused by changes in the reactor that took place between both experiments. For example, a 1 cm thick plate was installed on to the substrate holder, after the experiments in Chapter 3. This plate may

have caused some decrease in actual substrate temperature. Figure 3.8a shows that the resistivity would be very sensitive for a decrease in temperature, around 150 ^{o}C.

Figure 4.12b shows that the mobility decreased with increasing Al fraction. The TMA and DMAI curves were consistent with each other. Exceptions were the TMA value at 0 % and the DMAI value at approximately 11.6 %. These deviations from the general trend were ascribed to measurement errors. Measurement errors could possibly arise since the glass samples were too large for the Hall system. This could cause the Hall system magnetic field to be not completely uniform over the whole sample. This in turn, could result in a measurement error in free carrier concentration and mobility, while producing reasonable resistivity results. The silver paste contacts were placed somewhat further away from the sample edges to prevent this effect. However, the variation in silver paste contact positions, between different samples, may have caused some samples to be better than others.

Figure 4.12c shows that the free carrier concentration initially increased with increasing Al fraction. A sudden, steep decrease however, started between 10 and 15 %. This phenomenon was believed to be the cause of the rapid resistivity increase that started in the same Al fraction range.

Figure 4.12 showed that the resistivity initially decreased due to increasing carrier concentration. After reaching a minimum, the decrease in mobility became dominant and the resistivity started increasing again. A drop in carrier concentration finally added to the effect, causing a steep increase in resistivity. The trends in Figure 4.12 were generally consistent with the literature data shown in Figure 4.1. The DMAI process showed lower resistivity values up to an Al fraction of approximately 7.5 %. Note that the minimum resistivity values could be further improved by increasing the deposition temperature.

4.5.2 Field Effect Model

The formation of insulating Al_2O_3 clusters was mentioned in the literature as the main reason for the increasing resistivity with Al fraction [28,32]. The Al atoms that were bound in Al_2O_3, could not contribute free electrons anymore. In addition, Elam et al. found that dopants could perturb the ZnO lattice. This perturbation created scattering sites that decreased the electron mobility and ultimately increased the resistivity [32].

Do-Joong Lee et al. expanded the explanation of clustered Al_2O_3 with a field effect theory [30]. This theory provides a broader understanding of the mechanisms that affect the resistivity during Al doping of ZnO. *High angle annular dark field transmission electron spectroscopy* (HAADF TEM) was performed on AZO layers first. The HAADF TEM, in which the contrast of an image is formed from the mass difference between

elements, showed that the AZO films had a layered structure. This structure consisted of a ZnO matrix with intermediate, insulating Al_2O_3 layers, as shown in Figure 4.15. Extrinsic doping was believed to occur only at the interface of ZnO/Al_2O_3. Clustering between adjacent Al_2O_3 layers would hardly occur since these layers remained separated. Instead, a field effect as a result of the material structure was mentioned as additional mechanism that caused increased resistivity with increasing Al fraction.

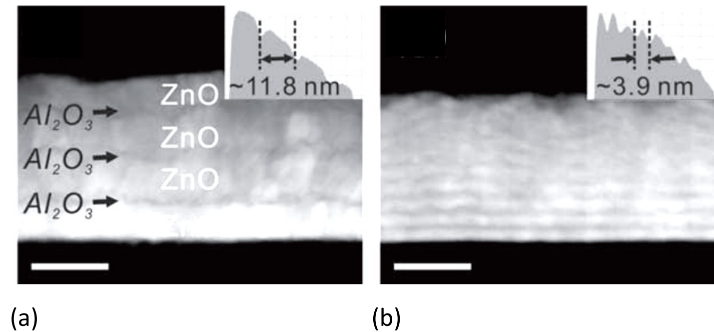

Figure 4.15 *HAADF TEM images of AZO films with different $ZnO:Al_2O_3$ cycle ratios (a) 49:1 (b) 19:1. The images show a structure consisting of a ZnO matrix with intermediate, insulating Al_2O_3 layers [30].*

The field effect is explained with Figure 4.16. Free electrons could be located within the Bohr radius around Al donors. Figure 4.16 shows the Al donors as blue dots and the electron Bohr radius as red spheres. Figure 4.16a shows the situation in which the Al_2O_3 planes are widely separated ($l > l_c$). This is the configuration in which electrons are most easily donated. Inserting additional Al_2O_3 planes, provides extra donated electrons, which is shown by Figure 4.16b. Further insertion of Al_2O_3 planes however, causes the Bohr radius of adjacent planes to overlap ($l < l_c$). In this situation the Coulombic repulsion force between donated electrons could suppress the donation of additional electrons. Note that that the planar spacing d between Al was estimated to be equal to l_c. The value of l_c was found to be 2.3-2.6 nm.

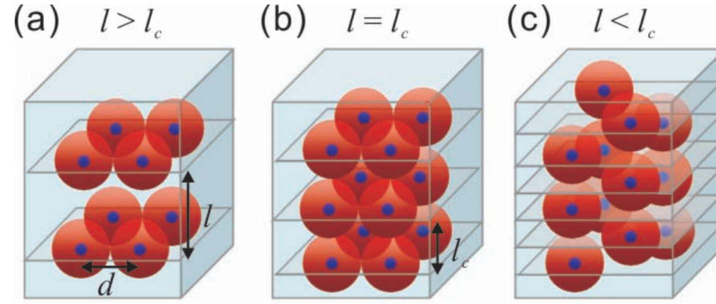

Figure 4.16 *Schematics of effective field model for AZO films. Blue dots and red spheres represent charged Al donors and free electron bohr radius. l is the interval between adjacent Al_2O_3 layers and l_c is the critical length just before the decrease of the carrier concentration (a) $l > l_c$ (b) $l = l_c$ (c) $l < l_c$ [30].*

Summarizing, the doped material was believed to consist of a ZnO matrix with intermediate, insulating Al_2O_3 layers. Carriers were donated at the ZnO/Al_2O_3 interface only. *d* and *l* were the characterizing parameters of the model and represented the planar spacing between Al atoms and the distance between Al_2O_3 layers respectively. When the Al_2O_3 layers are placed to close to each other, i.e. $l < l_c$, the field effect will terminate the donation of charge carriers. In the next section a method will be explained to determine the *l* and *d* values for the TMA and DMAI process. These quantities will then be related to the doping efficiency of both processes, which can be measured as well.

4.5.3 Doping Efficiency

The doping efficiency is the percentage of incorporated Al atoms that donate a carrier. The doping efficiency was calculated by:

$$\eta_{doping} = \frac{n - n_0}{\chi_{Al}} \cdot 100 \tag{4.5}$$

Where *n* is the free carrier concentration of the doped material, n_0 the free carrier concentration of the intrinsic material and χ_{Al} the number of Al atoms per cm^3 that was incorporated by doping. The values of *n* and n_0 were determined by Hall measurements. χ_{Al} was calculated by:

$$\chi_{Al} = \chi_{Zn} \cdot Al\% = \beta_{Zn} / t \cdot Al\% = 4 \cdot 10^{22} \cdot Al\% \tag{4.6}$$

Where χ_{Zn} is the number of Zn atoms per cm^3, *Al%* the XPS Al fraction, β_{Zn} the number of Zn atoms per cm^2 and *t* the thickness of the film. β_{Zn} was directly measured by RBS, for the intrinsic ZnO samples of thickness *t* in Chapter 3. Note that these samples were deposited at 100, 200 and 300 °C, as described in section 3.2.1. The RBS data was therefore interpolated to find the appropriate value of β_{Zn} at 150 °C, which was 308 atoms/cm^2. The average thickness was 77 nm, giving χ_{Zn} to be $4{\cdot}10^{22}$ atoms/cm^3.

Figure 4.17 shows the doping efficiency as a function of Al fraction. This figure shows that the doping efficiency decreases with increasing Al fraction. The field effect model of section 4.5.2 can be used to put the doping efficiency results into broader perspective.

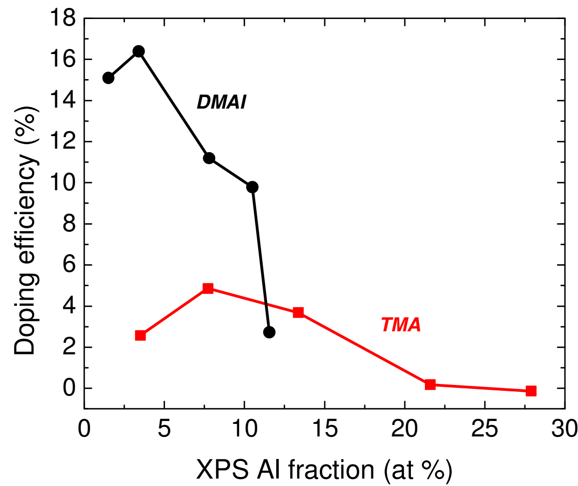

Figure 4.17 *Doping efficiency as a function of Al fraction. The doping efficiency decreases with Al fraction.*

The parameters of the field effect model were *d* and *l*. Figure 4.16 showed that *d* was the planar (horizontal) spacing between Al atoms and *l* was the vertical distance between Al_2O_3 layers. The values of *d* and *l* were calculated for the TMA and DMAI process.

The value of *l* was calculated by:

$$l = \frac{h}{k} \tag{4.7}$$

Where *h* is the sample thickness and *k* is the number of super-cycles.

The value of *d* was calculated by:

$$\frac{\chi_{Al} \cdot h}{k} = \frac{1}{d^2} \Leftrightarrow d = \frac{1}{\sqrt{\frac{\chi_{Al} \cdot h}{k}}} \tag{4.8}$$

Where $\frac{\chi_{Al} \cdot h}{k}$ represents the areal density of Al atoms per super-cycle. Note that within this calculation the Al atoms were assumed to be located within one monolayer, as described in the model of section 4.5.2. This model ignores the possible migration of Al atoms into the ZnO lattice. As a consequence, the calculated *d* values can be smaller than in reality.

The average values of *d* were found to be 0.30 $\pm$ 0.02 and 0.46 $\pm$ 0.02 nm for TMA and DMAI respectively. This means that the distance between Al atoms was larger for DMAI. This was probably caused by the steric hindrance effect that was described in section 4.4. The range of *l* was between 1 and 8 nm as will be showed later.

Figure 4.18 shows the doping efficiency as a function of *l*. The figure shows two important results. The first result is that the DMAI doping efficiency was generally higher at specific *l* values than that of TMA. This could be explained by the planar distance *d* between Al atoms. As described in section 4.5.2, donated electrons are located within the Bohr radius around the Al ion. When the Bohr radii of neighbouring Al atoms overlap, repulsion forces between electrons will oppose the donation of electrons. The calculation with equation (4.8) showed that DMAI has a larger planar distance *d* between adjacent Al atoms compared to TMA. This means less overlap of Bohr radii and subsequently a higher doping efficiency at equal distance *l* between Al_2O_3 layers.

The second result is the trend of the doping efficiency. Above a critical distance l_c between adjacent Al_2O_3 layers, the doping efficiency was expected to be constant. This means that the distance between Al_2O_3 layers was large enough, so that the layers did not interact by the field effect as explained in section 4.5.2. For values below the critical distance l_c, the doping efficiency was expected to be decreasing with decreasing *l* values. In this region the Al_2O_3 layers were close enough to each other, for the field effect to have influence. Figure 4.18 shows similar trends for TMA and DMAI. The doping efficiency of both processes seemed reasonably constant above *l* = 3.4 nm approximately, although an unambiguous conclusion that was based on only two data point was difficult. Below *l* = 3.4 nm, the doping efficiency decreased with decreasing *l* value. This behaviour was expected according to the field effect model. From this analysis one could say that the critical *l* value, l_c, was found to be 3.4 nm. The literature that was described in section 4.5.2 reported a value of 2.3-2.6 nm for TMA. Note that a

larger number of doping efficiency measurements would improve the accuracy of the preceding analysis.

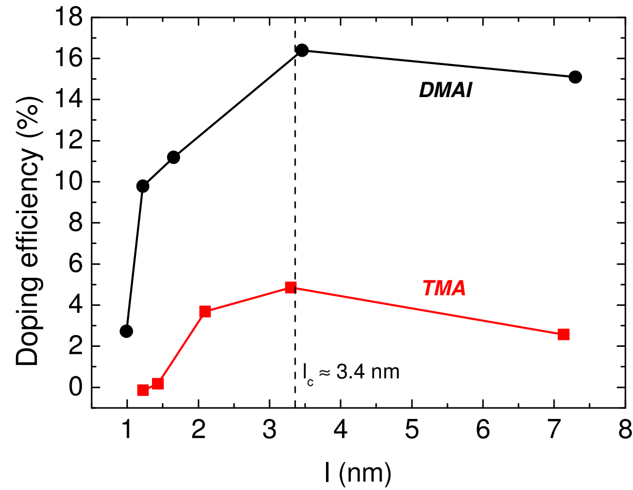

Figure 4.18 *Doping efficiency as a function l. For l values up to the critical value l_c, the doping efficiency increased. The field effect between Al_2O_3 layers caused the doping efficiency to be suppressed. Above the critical value l_c, the Al_2O_3 layers were separated far enough so that the field effect did not influence the donation of charge carriers anymore.*

4.6 Optical Properties

4.6.1 Transmittance

Figure 4.19 shows the measured transmittance for both TMA and DMAl series.

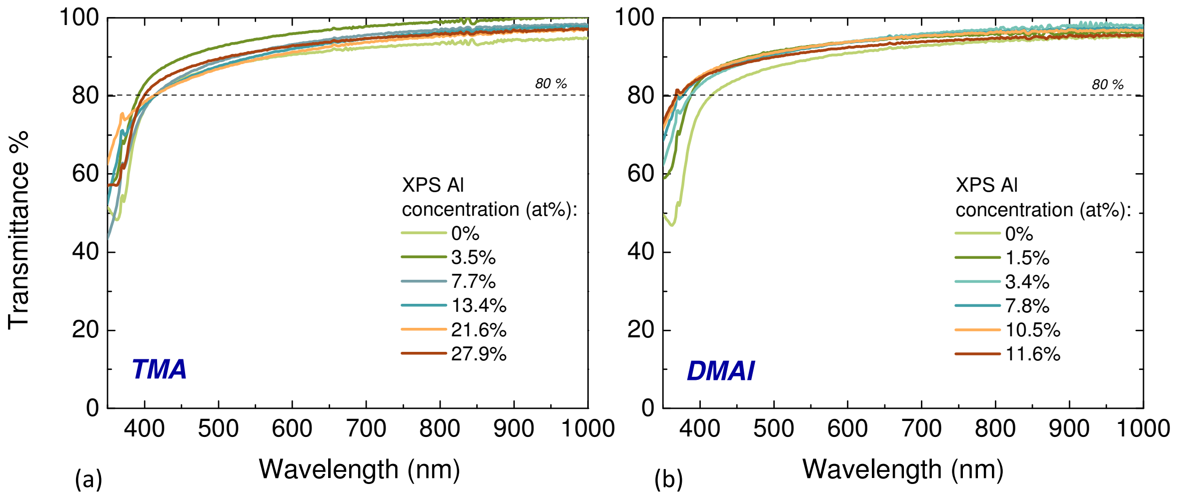

Figure 4.19 *Transmittance as a function of XPS Al fraction (a) TMA (b) DMAl*

Figure 4.19 shows that both TMA and DMAl processes produced layers with a transmittance above 80 %, in the range between approximately 400 and 1000 nm.

4.6.2 Optical Band Gap

Figure 3.19 shows $(\varepsilon_2 \cdot E^2)^2$ as a function of the photon energy E, for different Al fractions. The optical band gap (Tauc gap) is defined as the photon energy, where the extrapolation of the linear part of this parameter, intersects the line $(\varepsilon_2 \cdot E^2)^2 = 0$ [42]. Note that the dielectric functions were modelled by a B-spline. Figure 3.20 shows the values of the optical band gap as a function of Al fraction.

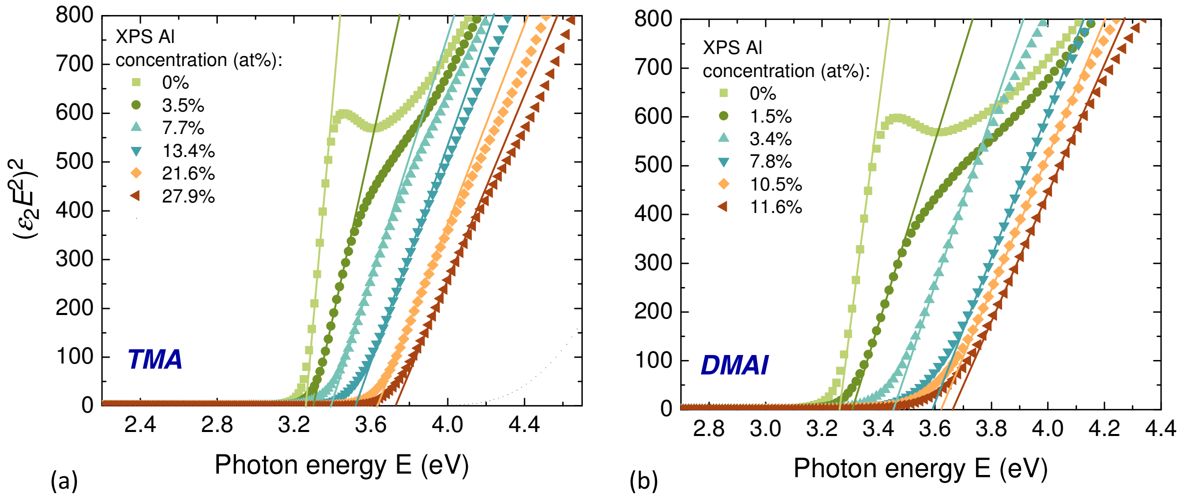

Figure 4.20 *$(\varepsilon_2 \cdot E^2)^2$ as a function of photon energy for different Al fractions. (a) TMA (b) DMAI.*

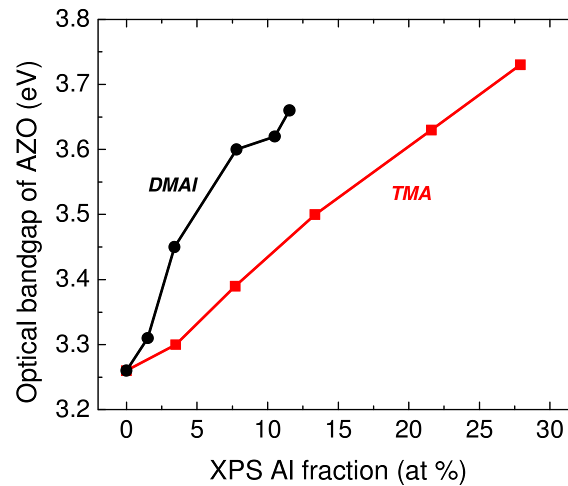

Figure 4.21 *Optical band gap as a function of Al fraction where (a) TMA (b) DMAI was the Al source*

Figures 4.20 and 4.21 show that the optical band gap increases with increasing Al fraction. The figures also show that the DMAI optical band gap is generally higher than the one of the TMA.

The increase of optical band gap with increasing Al fraction was ascribed in the literature to the Burstein-Moss shift [28,29], first reported by Burstein [54]. Free carriers

cause the Fermi level to increase. In the case of ZnO, when the free carrier concentration exceeds the limit of 10^{18} cm^{-3}, the semiconductor becomes fully degenerate. This means that the Fermi level lies above the conduction band. The optical band gap is defined as the energy that electrons gain when they interact with a photon. During this process the electrons in the valance band shift to unoccupied energy levels in the conduction band, which lie above the Fermi level. The Fermi level increases with free carrier concentration and therefore also the optical band gap increases. The principle is shown in Figure 4.21. Note that a carrier concentration of 10^{18} cm^{-3} is already present in intrinsic ZnO.

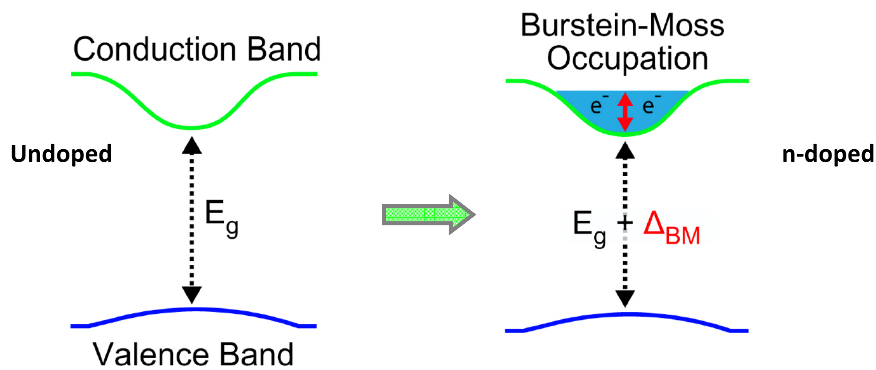

Figure 4.22 *Schematic presentation of Burnstein-Moss effect. .n-type donors cause the Fermi level to shift upwards, into the conduction band. The optical band gap is the energy that an electron gains when interacting with a photon. This energy increases with increasing Fermi level.*

The band gap of the DMAI process was higher than the TMA process since DMAI exhibited a higher doping efficiency, as was shown in section 4.5.3. This means that at a specific value of the Al fraction, DMAI donates more carriers than TMA. This was also shown in Figure 4.14c.

Note however, that Figure 4.14 shows that the carrier concentration decreased above Al fractions of approximately 12 %. This was due to Al_2O_3 clustering as described in section 4.5. The increasing band gap in the corresponding region of Figure 4.21, could therefore not be caused by the Burstein-Moss effect. Amorphous Al_2O_3 has an intrinsic band gap of 7-8 eV. The mixed composition of ZnO and Al_2O_3, with a band gap that is intermediate between these materials, may therefore be more likely to cause the band gap increase that was observed for Al fractions above approximately 12 %.

4.6.3 Spectroscopic Ellipsometry Material Library

The CompleteEASE SE software contains the functionality for constructing material files (OC libraries). A material file can be useful for samples that show a systematic shift in optical properties, related to material composition and/or temperature. The dielectric functions of samples with different compositions can be added to the material file. Information about the composition, that is independently acquired, can be added as well. The dielectric functions, together with the composition information comprises the reference data of the material file. CompleteEASE contains an interpolating algorithm. With this, an arbitrary dielectric function can be evaluated from a weighted sum of the nearest reference fucntions. This way the composition of the arbitrary sample can be found. SE measurements are relatively straightforward take and could potentially save a lot of (expensive) analysis, such as RBS.

Figures 4.23 and 4.24 show the dielectric function for the doped samples as a function of Al fraction, for TMA and DMAI respectively. The figures clearly show that the dielectric functions shift with increasing Al fraction. This property enables the construction of a material file within CompleteEASE.

Material files for TMA and DMAI were constructed. Dielectric functions were modelled by a B-spline, together with XPS Al fractions were used as reference data. With these material files, both the Al fraction and sample thickness of any doped layer could be found. Note that this only applied for samples that were deposited under similar conditions as the reference samples. The method only applies for the approximate Al fraction region of 0-30 and 0-12 % for TMA and DMAI respectively, since reference data was only added within this region. The material files could be further improved by using evenly spaced Al fractions as reference data, since that would provide an evenly spaced fitting uncertainty.

The constructed material files have not been not tested yet. Testing could be done by depositing samples with random Al fractions. The Al fractions could then be determined by the material library and compared to data from RBS or XPS. This comparison would tell whether the method is accurate enough.

Note that the TMA and DMAI material files are not interchangeable. Both processes exhibit different doping efficiencies. This means that, at a specific Al fraction, the processes exhibit different numbers of free carriers, causing the dielectric functions to be different.

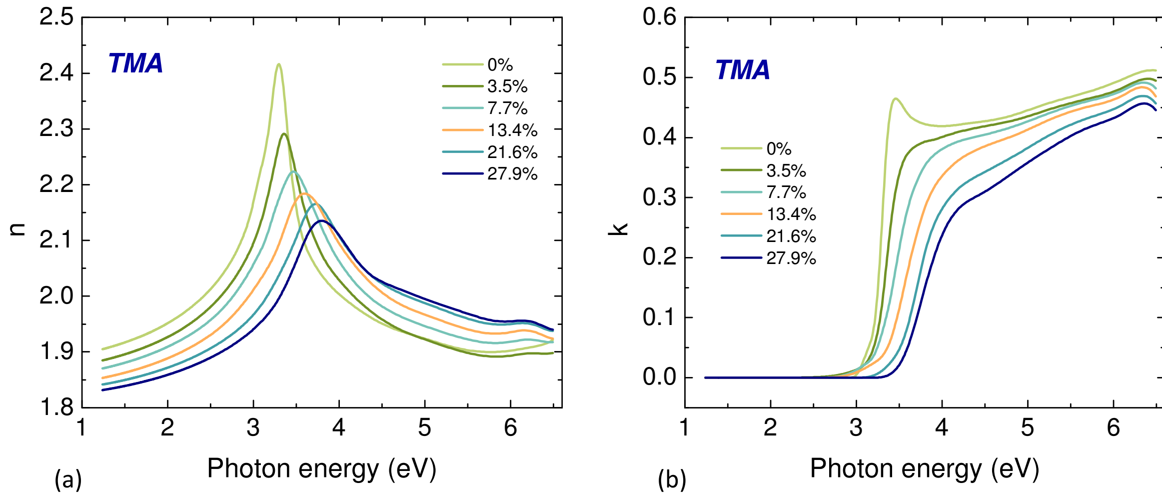

Figure 4.23 *Dielectric functions of AZO layers as a function of Al fraction, deposited with TMA as aluminium precursor (a) n (b) k.*

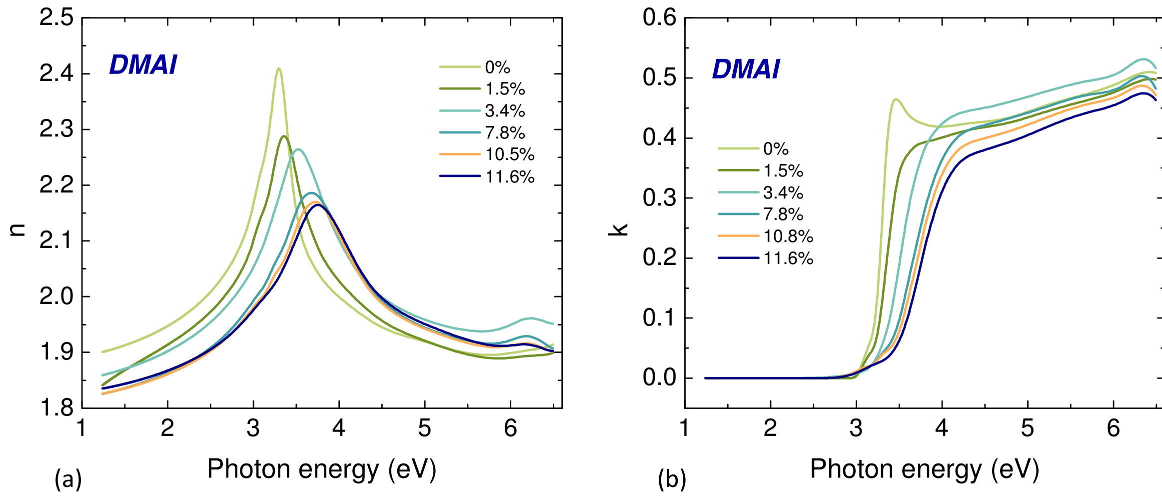

Figure 4.24 *Dielectric functions of AZO layers as a function of Al fraction, deposited with DMAI as aluminium precursor (a) n (b) k.*

4.7 Conclusions and Outlook

In this chapter, recipes were developed for aluminium doped ZnO. Both TMA and DMAI were used as aluminium precursors. In-situ SE was applied to study the growth mechanism. Aluminium incorporation, electrical and optical properties were studied by 4pp, Hall, RBS, XPS and SE.

The DMAI process showed a relatively strong growth inhibition in subsequent ZnO cycles. A hypothesis was formulated that could possibly explain this effect: The $OCH(CH_3)_2$ ligands of DMAI could remain present in the material after the second Al_2O_3 half cycle. These ligands could passivate OH groups and could also cause steric hindrance in subsequent ALD cycles. As a result, the ZnO growth could be inhibited more strongly after DMAI than after TMA.

Remaining ligands can be detected by XPS. A carbon depth profile for instance, could be measured for this purpose. Future XPS measurements could tell whether or not the hypothesis is true. An interesting question in this case would be whether or not the remaining ligands had any effect on resistivity or transmittance. Longer H_2O doses could be applied as an attempt to remove the remaining ligands. The resistivities and transmittance of the material, with and without remaining ligands, could than be compared in order to investigate if removing the ligands could further improve the DMAI doped ZnO process.

A second effect was that DMAI showed a higher doping efficiency than TMA, up to an Al fraction of approximately 12 %. Steric hindrance of the DMAI $OCH(CH_3)_2$ ligands, during the first half cycle, was likely to cause a wider spread of Al atoms than in the TMA process. This meant the electron repulsion forces were less dominant and more carriers could be donated. This advantage disappeared at Al fractions above 12 % due to the field effect between Al_2O_3 layers. The higher doping efficiency caused the resistivity of the DMAI process to be lower than that of TMA, at Al fractions up to approximately 12 %.

Note that both processes were not optimized for deposition temperature yet. Future substrate temperature optimization may greatly improve the minimum resistivities of both processes. Additional resistivity improvements could be acquired as well by fine-tuning of the optimal Al fraction. Future transmittance measurements could be taken in the spectral range above 1000 nm as well since the effect of doping might be better visible in this region. Such measurements would enable a better comparison of the precursors in terms of transmittance. A final suggestion would be to investigate the effect of post treatment. Annealing may cause the Al atoms to spread through the ZnO lattice. This may influence the doping efficiency for both methods, and therefore the electrical properties.

Regarding the SE material library, two suggestions can be made. First of all, it is expected that the library can be improved when more reference data is added. The additional data would preferably contain dielectric functions of samples with equally-paced, small step size Al fractions, in order to enhance the interpolation. The second suggestion would be to test the material library that was constructed. Samples with random Al fractions could be deposited and measured by both XPS/RBS and the SE library, to make comparison possible. This would tell whether the SE material library is an accurate method for determining the Al fraction.

Chapter 5

Conclusions and Outlook

ZnO is reported to be a promising candidate for many existing and novel thin film applications. An example is ZnO as TCO in solar cells, which needs high uniformity and thickness control. ALD is a thin film deposition technique that exhibits excellent uniformity, conformality and thickness control. This thesis concerned two main parts. The first part was development and characterization of both thermal and plasma-assisted ALD processes. The second part comprised the ALD of aluminium-doped ZnO, where both TMA and DMAI were used as aluminium precursors.

In the first part of the thesis, the thermal process showed a good *growth per cycle* (GPC) of 0.21 nm/cycle, non-uniformity of 3.3 % and minimum resistivity in the order of 10^{-2} Ωcm for 40 nm thick films. The thermal process was therefore considered to form a solid base for future research and applications.

The plasma-assisted process gave a GPC of 0.09 nm/cycle, non-uniformity of 22.3 %, a minimum resistivity in the order of 10^{1} Ωcm for 40 nm thick films and a long plasma dose of 16 s before saturation was reached. These results were not optimal for applications like TCOs. Therefore this process needs to be further optimized before the full potential of the plasma-assisted ALD process can be utilized. A suggestion would be to study the growth characteristics of the process more closely, i.e studying the saturation behaviour. Two experiments are proposed for this. First the O content of a series with different plasma dosing could be measured using RBS or XPS. This would tell whether a longer plasma dose incorporates extra O, which can cause additional growth. Secondly, depositions could be done with the plasma power turned off. This would tell whether O_2 acts as a reactant that causes an additional thermal growth component.

Although excellent results were achieved with the thermal ALD process, the material resistivity could be further improved. This could be done by Al doping for instance, which was the subject of the second part of the thesis. A number of papers already exist on the thermal ALD of Al-doped ZnO, which reported the use of *trimethyl-aluminium* (TMA) as the Al precursor. TMA however, is pyrophoric and therefore carries potential safety risks when it is applied in high scale industrial applications. *Dimethyl-aluminium isoproxide* (DMAI) is a relatively new Al precursor that is not pyrophoric. In this thesis ALD processes of Al-doped ZnO were developed, where both TMA and DMAI were used. The use of both precursors was then compared in terms of growth, aluminium incorporation, electrical and optical properties. Note that the aluminium-doping was only studied for the thermal process since the intrinsic plasma-assisted process showed much higher resistivity values than the intrinsic thermal process.

The DMAI process showed a relatively strong growth inhibition in subsequent ZnO cycles. A hypothesis was formulated that could possibly explain this effect. The hypothesis stated that $OCH(CH_3)_2$ ligands of DMAI could remain present in the material after the second Al_2O_3 half cycle. These ligands could passivate OH groups and could also cause steric hindrance in subsequent ALD cycles. As a result, the ZnO growth could be inhibited more strongly after DMAI than after TMA.

Remaining ligands can be detected by XPS which would conform the pypothesis. A carbon depth profile for instance, could be measured for this purpose. Future XPS measurements could tell whether or not the hypothesis is true. An interesting question in case when the hypothesis is true would be whether or not the remaining ligands had any effect on resistivity or transmittance. Longer H_2O doses could be applied as an attempt to remove the remaining ligands. The resistivities and transmittance of the material, with and without remaining ligands, could than be compared in order to investigate if removing the ligands could further improve the DMAI doped ZnO process.

A second effect was that DMAI showed a higher doping efficiency than TMA, up to an Al fraction of approximately 12 %. Steric hindrance of the $OCH(CH_3)_2$ ligands, during the first half cycle, was likely to cause the Al atoms to be more sparsely located throughout the material than in the TMA process. This meant the electron repulsion forces were less dominant and more carriers could be donated. This advantage disappeared at Al fractions above 12 % due to the field effect between Al_2O_3 layers. The higher doping efficiency caused the resistivity of the DMAI process to be lower than that of TMA, at Al fractions up to approximately 12 %.

Note that both processes had not been optimized for deposition temperature. Future substrate temperature optimization may greatly improve the minimum resistivities of both doping processes. Additional resistivity improvements could be acquired as well by fine-tuning of the optimal Al fraction. Future transmittance measurements can be taken in the spectral range above 1000 nm as well since the effect of doping might be better visible in this region. Such measurements would enable a better comparison of the precursors in terms of transmittance. A final suggestion would be to investigate the effect of post treatment. Annealing may cause the Al atoms to spread through the ZnO lattice. This may influence the doping efficiency for both methods, and therefore the electrical properties.

The higher doping efficiency, with resulting lower resistivity, is the reason that DMAI is currently regarded to be a better Al precursor than TMA for use in TCO applications.

Acknowledgements

The moment has finally come to start thanking people ☺. First I like to thank my supervisor Stephen. Stephen, although you wear glasses, I must say that you had eagle eyes when it came to finding spelling errors in my report and this helped me a lot in difficult formulations. I would also like to thank Erwin. Despite your busy schedule you found the opportunity to provide useful and profound comments and this was an important contribution to my work. A contest was also held in the students' room. I am the appointed person to inform you that you were elected to have the coolest hair style of all professors, a great honor! ☺

I am very happy with the feedback I received from the people in our group. Thanks in particular to Harm and Diana where I could always drop by the office to ask questions, to Harald who taught me how to use the ALD reactor, to Wytze who did XRD measurements for me and sold me some great reading books and of course to Christian, who was patient enough to force a smile on his face when we found that he needed to sand-blast the reactor for the second time, after some unfortunate experiments. Also many thanks to Jan-Willem and Valentino for helping me with SE modeling, which was not always straightforward for ZnO. Special thanks go out to Yizhi. You really showed great interest in my work and reached out to give advice whenever possible. You also did important XPS measurements for me and above all, I feel we became good friends in the process.

Thanks as well to my fellow students who created a great working atmosphere. Erik, thanks for drowning me in beer from time to time. Thanks to you I realize I can really push boundaries in life! Special thanks to Martijn and Jonathan. You guys were very close to me and I am happy with all the moments we shared inside and outside the university.

Finally I want to say that pmp is a great group and that I really had a good time!

Appendix A

Precursor Properties

Table A.1 *Properties of DEZ, TMA and DMAI*

Precursor property	DEZ	TMA	DMAI
Physical state (R.T.)	Liquid	Liquid	Liquid
Melting point	-28 °C	15 ^{o}C	< R.T.
Boiling point	118 °C	125 ^{o}C	172 ^{o}C
Decomposition temperature	>200 °C	~330 ^{o}C	~370 ^{o}C
Vapour pressure	9 Torr at 15 ^{o}C	9 Torr at 17 ^{o}C	9 Torr at 67 ^{o}C
Pyrophoric	Yes	Yes	No

Appendix B

Recipes of ZnO & Al_2O_3 Processes

Table B.1 *Recipe of thermal ALD process of ZnO at 150 ^oC deposition temperature*

	DEZ dose 30 ms	DEZ purge 5 s	H_2O dose 20 ms	H_2O purge 6 s
DEZ	on	off	off	off
H_2O	0	0	1	0
Ar gate valve (sccm)	150	0	150	0
Ar through DEZ (sccm)	0	150	0	0
Ar through H_2O (sccm)	0	0	0	150
gate valve	0	0	0	0

Table B.2 *Recipe of plasma-assisted ALD process of ZnO at 150 ^oC deposition temperature*

	DEZ dose 30 ms	DEZ purge 1 s	Remove N_2 + O_2 build up 5 s	O_2 plasma dose 4 s	O_2 plasma purge 6 s
DEZ	on	off	off	off	off
O_2 (sccm)	0	0	50	50	0
N_2 (sccm)	100	100	0	0	100
Ar gate valve (sccm)	70	0	100	100	70
Ar through DEZ (sccm)	0	100	0	0	0
Plasma power (W)	0	0	0	200	0
Plasma source mode	HOLD	HOLD	HOLD	HOLD	HOLD
gate valve	1	1	1	1	1

Table B.3 *Recipe of Al_2O_3, thermal ALD process with TMA at 150 ^oC deposition temperature*

	TMA dose 20 ms	TMA purge 3.5 s	H_2O dose 20 ms	H_2O purge 3.5 s
TMA	on	off	off	off
H_2O	0	0	1	0
Ar through TMA (sccm)	0	150	150	0
Ar through H_2O (sccm)	150	0	0	150
gate valve	0	0	0	0

Table B.4 *Recipe of Al_2O_3, plasma-assisted ALD process with TMA at 150 ^oC deposition temperature*

	TMA dose 20 ms	TMA purge 3.5 s	O_2 plasma dose 4 s	O_2 plasma purge 0.5 s
TMA	on	off	off	off
O_2 (sccm)	50	50	50	50
Ar through TMA (sccm)	0	100	100	0
Ar through H_2O (sccm)	100	0	0	100
Plasma power (W)	0	0	200	0
Plasma source mode	HOLD	HOLD	HOLD	HOLD
gate valve	1	1	1	1

Table B.5 *Recipe of Al_2O_3, thermal ALD process with DMAI*

	DMAI dose 500 ms	**DMAI purge 10 s**	**H_2O dose 30 ms**	**H_2O purge 10 s**
DMAI	on	off	off	off
H_2O	0	0	1	0
Ar through DMAI bubbler (sccm)	50	200	200	0
Ar through DMAI (sccm)	0	0	0	0
Ar through H_2O (sccm)	200	0	0	200
gate valve	0	0	0	0

Table B.6 *Recipe of Al_2O_3, plasma-assisted ALD process with DMAI*

	DMAI dose 500 ms	**DMAI purge 10 s**	**O_2 plasma dose 4 s**	**O_2 plasma purge 10 s**
DMAI	on	off	off	off
O_2 (sccm)	50	50	50	50
Ar through DMAI bubbler (sccm)	50	20	0	0
Ar through DMAI (sccm)	0	0	100	0
Ar through H_2O (sccm)	20	0	20	20
Plasma power (W)	0	0	200	0
Plasma source mode	HOLD	HOLD	HOLD	HOLD
gate valve	1	1	1	1

Bibliography

[1] K. Ellmer, A. Klein, B. Rech, *Transparent Conductive Zinc Oxide*, Chs. 1 & 8, Springer-Verlag, Berlin (2008).

[2] C. Klingshirn, *Phys. Stat. Sol.*, **244**, 3027– 3073 (2007).

[3] N. Izyumskaya, V. Avrutin, Ü. Özgür, Y. I. Alivov, and H. Morkoç, P*hys. Stat. Sol.*, **244**, 1439 – 1450 (2007).

[4] L. Schmidt-Mende, J.L. MacManus-Driscoll, *Mater. Today*, **10**, 40-46 (2007).

[5] A. Janotti, C.G. Van de Walle, *Rep. Prog. Phys.*, **72**, 126501 (2009).

[6] Ü. Özgür, D. Hofstetter, H. Morkoc, *Proc. IEEE*, **98**, 1255-1268 (2010).

[7] S. De Wolf, A. Descoeudres, Z.C. Holman, C. Ballif, *Green*, **2**, pp. 7–24 (2012).

[8] W. Beyer, J. Hüpkes, H. Stiebig, *Thin Solid Films*, **516**, 147 – 154 (2007).

[9] D.K. Schroder, *Semiconductor Material and Device Characterization*, Chs. 1 & 8, John Wiley & Sons, New Jersey (2006).

[10] A.E. Delahoy, S. Guo, *Handbook of Photovoltaic Science and Engineering*, Ch. 17, Wiley & Sons, New Jersey (2011).

[11] E. Fortunato, D. Ginley, H. Hosono, D.C. Paine, *MRS. Bul.*, **32**, 242-247 (2007).

[12] D. Inamdar, C. Agashe, P. Kadam, S. Mahamuni, *Thin Solid Films*, **520**, 3871–3877 (2012).

[13] C. Agashe, O. Kluth, G. Schope, H. Siekmann, J. Hupkes, B. Rech, *Thin Solid Films*, **442**, 167–172 (2003).

[14] P.D.C. King, T.D. Veal, *J. Phys.: Condens. Matter*, **23**, 334214 (2011).

[15] S.M. George, *Chem. Rev.*, **2010**, 111–131 (2009).

[16] H.B. Profijt, S.E. Potts, M.C.M. van de Sanden, W.M.M. Kessels, *J. Vac. Sci. Technol. A*, **29**, (2011).

[17] T. Suntola, *Mat. Sci. Rep.*, **4**, 261-312 (1989).

[18] R.L. Puurunen, *J. Appl. Phys.,* **97**, 121301 (2005).

[19] R.L. Puurunen, *Chem. Vap. Dep.*, **2003**, 249-257 (2003).

[20] D. Kim, H. Kang, J. Kim, H. Kim, *Appl. Surf. Sci.*, **257**, 3776–3779 (2011).

[21] G. Luka, T. Krajewsk, L. Wachnicki, B. Witkowski, E. Lusakowska, W. Paszkowicz, E. Guziewicz, M. Godlewski, *Phys. Stat. Sol. A*, **207**, 1568–1571 (2010).

[22] S.K. Kim, C.S. Hwang, S.K. Park, S.J. Yun, *Thin Solid Films*, **478**, 103 – 108 (2005).

[23] E. Guziewicz, I.A. Kowalik, M. Godlewski, K. Kopalko, V. Osinniy, A. Wójcik, S. Yatsunenko, E. Łusakowska, W. Paszkowicz, M. Guziewicz, *J. Appl. Phys*, **103**, 033515 (2008).

[24] S.K Park, C. Hwang, H Kwack, J. Lee, H.Y. Chu, *Electrochem. Solid-State Lett*, **9**, G299-G301 (2006).

[25] S. Jeon, S. Bang, S. Lee, S. Kwon, W. Jeong, H. Jeon, H.J. Chang, H. Park, *J. Electrochem. Soc.*, **155**, H738-H743 (2008).

[26] T. Nam, J. Kim, M. Kim, H. Kim, *J. Korean Phys. Soc.*, **59**, 452~457 (2011).

[27] A. Yamada, B. Sang, M. Konagai, *Appl. Surf. Sci.*, **112**, 216-222 (1997).

[28] C.H. Ahn, H. Kim, H.K. Cho, *Thin Solid Films*, **519**, 747– 750 (2010).

[29] P. Banerjee, W. Lee, K. Bae, S.B. Lee, G.W. Rubloff, *J. Appl. Phys*, **108**, 043504 (2010).

[30] D. Lee , H. Kim, J. Kwon, H. Choi, S. Kim, K. Kim, *Adv. Funct. Mater.*, **2011**, 448-455 (2011).

[31] J.W. Elam, S.M. George, *Chem. Mater.*, **2003**, 15, 1020-1028 (2002).

[32] J.W. Elam, D. Routkevitch, S.M. George, *J. Electrochem. Soc.,* **150**, G339-G347 (2003).

[33] J.W. Elam, Z.A. Sechrist, S.M. George, *Thin Solid Films*, **414**, 43–55 (2002).

[34] H. Saarenpaa, T. Niemi, A. Tukiainen, H. Lemmetyinen, N. Tkachenko, *Sol. Energy Mat. Sol. Cells*, **94**, 1379–1383 (2010).

[35] V. Lujala, J. Skarp, M. Tammenmaa, T. Suntola, *Appl. Surf. Sci.*, **82**, 34-40 (1994).

[36] J. Na, G. Scarel, G.N. Parsons, *J. Phys. Chem. C*, **2010**, 383–388 (2009).

[37] J.Y Kim, Y. Choi, H. Park, *J. Vac. Sci. Technol. A*, **28**, 0734-2101 (2010).

[38] H. Yuan, B. Luo, D. Yu, A. Cheng, S.A. Campbell, W.L. Gladfelter, *J. Vac. Sci. Technol. A*, **30**, 0734-2101 (2012).

[39] Z.s. Baji, Z. Labadi, Z.E. Horvath, M. Fried, B. Szentpali, I. Barsony, *J. Therm. Anal. Calorim*, **105**, 93–99 (2011).

[40] N.P. Dasgupta, S. Neubert, W. Lee, O. Trejo, J. Lee, F.B. Prinz, *Chem. Mater.*, **2010**, 4769–4775 (2010).

[41] T. Dhakal, D. Vanhart, R. Christian, A. Nandur, A. Sharma, C.R. Westgate, *J. Vac. Sci. Technol. A*, **30**, 0734-2101 (2012).

[42] E. Langereis, S.B.S. Heil, H.C.M. Knoops, W. Keuning, M.C.M van de Sanden, W.M.M. Kessels, *J. Phys. D: Appl. Phys.*, **42**, 073001 (2009).

[43] H. Fujiwara, *Spectroscopic Ellipsometry*, Ch. 5, John Wiley & Sons, New Jersey (2007).

[44] C. Kittel, *Introduction to Solid State Physics*, Ch. 2, John Wiley & Sons, New Jersey (2005).

[45] R. Matero, A. Rahtu, M. Ritala, M. Leskela, T. Sajavaara, *Thin Solid Films*, **368**, 1-7 (2000).

[46] L. Henn-Lecordier, M. Anderle, E. Robertson, G.W. Rubloff, *J. Vac. Sci. Technol. A*, **29**, 0734-2101 (2011).

[47] O. Nilsen, O.B. Karlsen, A. Kjekshus, H. Fjellvåg, *Thin Solid Films*, **515**, 4527-4558 (2007).

[48] J.L. van Hemmen, S.B.S. Heil, J.H. Klootwijk, F. Roozeboom, C.J. Hodson, M.C.M. van de Sanden, W.M.M. Kessels, *J. Electrochem. Soc.*, **154**, G165-G169 (2007).

[49] S.E. Potts, W. Keuning, E. Langereis, G. Dingemans, M.C.M. van de Sanden, W.M.M. Kessels, *J. Electrochem. Soc.*, **157** , P66-P74 (2010).

[50] K. Elers, T. Blomberg, M. Peussa, B. Aitchison, S. Haukka , S. Marcus, *Chem. Vap. Dep.*, **2006**, 13-24 (2006).

[51] S.E. Potts, G. Dingemans, C. Lachaud, W.M.M Kessels *J. Vac. Sci. Tech. A,* **30**, 021505 (2012).

[52] V. Longo, N. Leick, F. Roozeboom, W.M.M. Kessels, *ECS Trans.*, **41**, 63-72 (2011).

[53] W.M. Baynes, *Handbook of Chemistry and Physics*, Bond Dissociation Energies, CRC Press (2012).

[54] E. Burstein, Anamalous Optical Absorption Limit in InSb in *Letters to the Editor* (1953)